Product state distributions in the dissociation of H_3 ($n=2,3$) Rydberg states

U. Müller[a] and P. C. Cosby
Molecular Physics Laboratory, SRI International, Menlo Park, California 94025

(Received 23 April 1996; accepted 16 May 1996)

Dissociation of the $2s\ ^2A_1'$, $2p\ ^2A_2''$, $3s\ ^2A_1'$, and $3d\ ^2E''$ Rydberg states of the H_3 molecule is investigated using a fast neutral beam photofragment spectrometer. A beam of 3–6 keV metastable H_3 $2p\ ^2A_2''$ ($N=K=0$) molecules, generated by charge transfer neutralization of H_3^+ ions in Cs vapor, is intersected by a laser beam to selectively populate a specific rovibrational level in each of the H_3 states for study. The correlated pair of fragments $H+H_2$, created by dissociation of the H_3 state, is observed by a time- and position-sensitive detector, which specifies the fragments' center-of-mass kinetic energy release and angle of ejection. The $3s\ ^2A_1'$ ($N=1$, $K=0$) and $3d\ ^2E''$ ($N=1$, $G=0$, $R=1$) rotational levels are prepared either in their ground vibrational states or in vibrationally excited states by pumping transitions from the $2p\ ^2A_2''$ ($N=K=0$) level with a tunable dye laser. All of these photoexcited levels are observed to both predissociate and to radiate into the dissociative ground state. In contrast, the $2s\ ^2A_1'$ ($N=1$, $K=0$) level, produced by stimulated emission pumping from the $2p\ ^2A_2''$ ($N=K=0$) level using a CO_2 laser, is observed to only predissociate. Predissociation of the H_3 produces a discrete release of kinetic energy to the $H+H_2$ fragments that uniquely identifies the production of a specific rovibrational level in the H_2. Monte Carlo simulation of the detector response, combined with observation of the corresponding dissociations in D_3 (where predissociation is essentially negligible), allows quantitative separation of $H+H_2$ predissociation fragments from a background of continuous energy release produced by radiative dissociation. Branching ratios in the radiative and the predissociative decay channels are estimated and detailed distributions for the production of the $H_2(v,J)$ final state are determined. Comparison of experimental distributions with recent theoretical calculations illuminates the important role nonlinear couplings play in determining the dissociation dynamics of a particular H_3 Rydberg state. Additionally, transition energies for the vibrationally excited levels of H_3 are determined with improved accuracy, the relative importance of the H+H+H dissociation channel is estimated, and spontaneous dissociation of the metastable $2p\ ^2A_2''$ ($N=K=0$) level is discussed.
 [S0021-9606(96)02232-5]

I. INTRODUCTION

The conceptual simplicity of a triatomic molecule formed by three hydrogen atoms has given the H_3 molecule a unique role in the development of modern quantum chemistry. The ground electronic configuration of this molecule, which is unbound,[1] has been probed by a series of increasingly sophisticated, and now state specific, measurements[2–10] and quantum calculations[11–14] of the hydrogen exchange reaction. In contrast, excited electronic configurations of the three hydrogen atoms yield strongly bound H_3 molecular states that are best viewed as a weakly bound Rydberg electron orbiting a tightly bound H_3^+ ion core.[15–19] This Rydberg character of the H_3 allows its facile production by ion-molecule charge transfer reactions wherein an electron is captured by the H_3^+ reactant.

Photoemission spectra due to transitions between Rydberg levels with $n=2$ and $n=3$ have been observed by Herzberg's group in electrical glow discharges and have yielded a detailed understanding of the electronic structure in those states.[20–23] Molecular beam studies of H_3 have been made by viewing the temporal and spectral distribution of the H_3^* photoemission following the charge transfer neutralization of H_3^+ in either alkali atom vapor or H_2 gas, and both bound–bound[24–26] and bound–free[27,28] transitions have been observed. Since all of the electronically excited states of H_3 lie in the vibrational continuum of the repulsive ground electronic state, rapid predissociation of these states is expected and its effects have been observed both in the width of the spectral lines[23] and in the temporal decay of the emission.[25,26] The existence of a long-lived (metastable) level of the triatomic hydrogen molecule was discovered in fast-beam experiments.[29–32] This rotationless $2p\ ^2A_2'$ ($N=K=0$) level is not vibronically coupled to the dissociative $\tilde{X}\ 2p\ ^2E'$ ground state,[33] a fact that allows a sufficiently long lifetime, 640 ns for the ground vibrational level,[34] for the $2p\ ^2A_2''$ ($N=K=0$) level to be used as a platform for laser excitation experiments that have explored the spectroscopy of the higher Rydberg levels using various laser-excitation schemes.[34–44] In addition, laser excitation from this metastable level has allowed the predissociation of the lower Rydberg states to be examined.[45–47]

The objective of the present investigation is to study the various dissociation channels of laser-prepared rotational and vibrational levels in the $2s\ ^2A_1'$, $3s\ ^2A_1'$, and $3d\ ^2E''$ Rydberg states of H_3 using photofragment spectroscopy. Predissociation of a single energy level of the H_3 to produce $H+H_2$ products must release a kinetic energy to these products that

[a]Present address: Universität Freiburg, Fakultät für Physik, Hermann-Herder Str. 3, D-79104 Freiburg, Germany.

is exactly equal to the difference in the potential energies of the H_3 level and the H_2 product. Since the potential energy of the H_2 product is simply the energy of the rovibrational level in which it is produced, a precise measurement of this kinetic energy release, which we represent by W, fully specifies the rotational and vibrational quantum numbers of the product H_2. This paper presents quantitative distributions of the $H_2(v,J)$ product levels produced in the predissociation of each of these Rydberg states in their ground vibrational levels, and in vibrationally excited levels for two of the states. In addition the branching between predissociation and emission is measured for these states. The present measurements allow comparison with the product distribution predicted by *ab initio* calculations of the H_3 dissociations[48–50] and provide an experimental base to guide improvements in the theory describing the dissociation dynamics.

II. EXPERIMENT

The experimental setup is similar to that reported in previous publications from this laboratory[51] and will be discussed in brief. Rotationally and vibrationally cold H_3^+ ions were created in a hollow cathode discharge source. The hydrogen pressure in the source was about 1 Torr and the cathode was cooled to a temperature of about 240 K. The ions were extracted from the plasma by a weak electric field through an aperture of about 100 μm in diameter, accelerated to energies between 3 and 6 keV, and mass selected by a magnetic sector. Typical ratios of the H_3^+ and H_2^+ ion currents produced by the source were in the range of 5:1 to 10:1. The H_3^+ beam enters an oven containing cesium vapor and a fraction ($<10\%$) is neutralized by charge transfer:

$$H_3^+ + Cs \rightarrow H_3^* + Cs^+. \tag{1}$$

Unreacted ions passing through the cell are removed from the beam by a weak electric deflection field. The H_3^* products of reaction (1) are produced in a distribution of $n=2$, and 3 Rydberg states by near-resonant charge transfer. Nearly all of these states rapidly predissociate to produce fast $H+H_2$ dissociative charge transfer products. However, a single H_3 quantum state, the $2p\ ^2A_2''$ ($N=K=0$), is sufficiently long-lived[34] (640 ns) to provide a platform for the present experiments. Experiments were also performed on the D_3 isotope. This was produced in the same manner as for H_3, by operating the ion source with D_2 gas. The yield of the metastable $2p\ ^2A_2''$ ($N=K=0$) state in D_3, however, is significantly less than in H_3($\sim 10\%$) due to the difference in nuclear spin statistics of the two species.[32]

Separation of the metastable H_3 beam from the dissociative charge transfer products is accomplished by passing the neutral beam through a narrow (500 μm) slit located 54 cm downstream from the charge transfer cell. All neutrals passing through this slit are intercepted by a 1.2 mm wide beam flag positioned 10 cm downstream from the slit. However, if a neutral molecule dissociates within this 10 cm interval to produce fragments with sufficient velocity transverse to the beam direction, these fragments can escape collection by the beam flag and travel an additional 100 cm to the detector.

Correlated photofragment pairs produced by the dissociation of individual molecules were detected in coincidence by a time- and position-sensitive detector located about 110 cm from the interaction region. The detector is similar to that reported by deBruijn and Los[52] and was discussed in detail by Helm and Cosby.[51] For each dissociation event, the radial distances R_1 and R_2 of the fragment impacts from the detector center and the arrival time difference ($\Delta t = t_2 - t_1$) are measured. The ratio Z,

$$Z \equiv \frac{R_1}{R_2}\left(1 - \frac{v_0 \Delta t}{L_0}\right) \approx \frac{m_2}{m_1}, \tag{2}$$

allows us to determine the fragment masses m_1 and m_2 from the known mass M of the parent molecule. Using the primary beam energy E_0, the beam velocity $v_0 = \sqrt{2E_0/M}$, and the distance between the interaction region and the detector L_0, the spatial ($R = R_1 + R_2$) and temporal (Δt) separations between the fragments at the detector also define both the fragment ejection angle θ,

$$\tan(\theta) = \frac{v_0 \Delta t}{R}, \tag{3}$$

and the kinetic energy release W,

$$W = E_0 \frac{m_1 m_2}{M^2} \frac{R^2 + (v_0 \Delta t)^2}{L_0^2}\left(1 - 2\frac{v_0 \Delta t}{L_0}\frac{|m_2 - m_1|}{M}\right). \tag{4}$$

which are evaluated on line by the laboratory computer and are presented as histograms in the present work. A precise calibration of the detector radial distances together with a somewhat longer flight length L_0 affords roughly a factor of 2 better resolution in W than was achieved in earlier work.[46]

Two lasers were used in the present experiments. Visible transitions into the $3s$ and $3d$ levels of the H_3 molecule were accessed using a dye laser (Rhodamine 6G) pumped by an argon-ion laser. The dye laser was operated with an extended cavity whose ~ 2 mm diameter beam intersected the H_3 beam approximately 2 mm downstream from the slit, with the electric vector of the linearly polarized laser perpendicular to the velocity of the H_3 beam. For the wavelength scans, only a birefringent filter, tuned by a stepping motor under computer control, provided the wavelength selective element. This yielded a linewidth for the laser of ~ 1 cm^{-1}. For acquisition of fragment kinetic energy distributions at a selected laser wavelength, an angle-tuned, 0.1 mm thick solid etalon was also included in the laser cavity. The etalon narrowed the laser linewidth to <0.1 cm^{-1}. In either configuration, the typical intracavity laser power was ~ 25 W. A fraction of the laser light was coupled into a wavemeter (Burleigh, Wavemeter jr) which was connected to the laboratory computer by a serial interface. The calibration of the wavemeter was performed by a HeNe laser. We estimate a combined uncertainty of 0.3 cm^{-1} for the wavelength measurements.

For stimulated emission pumping of the H_3 molecule into the $2s$ state, we used a single mode CW-CO_2 laser (ADKIN, MIRL-50 CW). The wavelength of the laser was monitored by a calibrated grating spectrograph. With a flat

end mirror, the laser was operating on a single, strong line [$P(20)$ of the $(00^01)-(10^00)$ vibrational transition of $^{12}C^{16}O_2$] at a wavelength of 10.6 μm with a power of ~10 W. The laser beam intercepted the H_3 beam in three passes at distances between 0.2 and 1 cm downstream from the slit. The laser beam was linearly polarized and its electric vector could be oriented either parallel or perpendicular to the velocity of the H_3 beam.

The $2p\ ^2A_2''$ ($N=K=0$) metastable state dissociates with a lifetime of about 640 ns.[34] Fragment pairs, produced by this dissociation taking place within the region bounded by the slit and the beam flag, yield a kinetic energy release in the range $0.5 \leqslant W \leqslant 5.5$ eV.[46] These spontaneous dissociation fragments constitute a background to the photodissociation measurements. To distinguish between the photofragments and the spontaneous dissociation fragments, the laser beam was chopped with a 50% duty cycle by a computer-controlled shutter, and multichannel spectra of the kinetic energy release W were collected separately during the laser-on and laser-off periods. Since the metastable beam is depleted appreciably by the laser-excitation process, the laser-off signal has to be weighted appropriately before its subtraction from the laser-on spectrum and this weight factor must be derived from physical considerations. Therefore, the laser-on and laser-off spectra were stored separately for further data treatment on a workstation.

III. RESULTS

A. Experimental spectra

As pointed out by Dabrowski and Herzberg,[20] the selection rules for optical dipole radiation in a parallel transition between nondegenerate states of H_3 are $\Delta K=0$, $\Delta N=0, \pm 1$. Starting from the metastable $2p\ ^2A_2''$ ($N=K=0$) state, rotational levels with quantum numbers ($N=1$, $K=0$) of the np^2A_1' Rydberg series can be excited. The selection rules for transitions into degenerate electronic states are $\Delta N=0, \pm 1$ and $\Delta G=0$,[23] which allows us to pump ($N'=1$, $G'=0$) rotational states of the nd^2E'' Rydberg series. In Fig. 1 the photofragment flux in the 3.5–8 eV kinetic energy release range was recorded as a function of the laser wavelength. As reported in a previous study from this laboratory,[46] the wavelength scan shows two strong and four weaker lines. In Table I, the observed transition frequencies are listed along with their spectroscopic labeling. The strong features at 17 296.6 cm^{-1} and 16 695.2 cm^{-1} have been observed in emission[20,23] and can be assigned to the $3s\ ^2A_1'\ \nu_0$ ($N=1$, $K=0$)$\leftarrow 2p\ ^2A_2''\ \nu_0$ ($N=K=0$) and $3d\ ^2E''\ \nu_0$ ($N=1$, $G=0$, $R=1$)$\leftarrow 2p\ ^2A_2''\ \nu_0$ ($N=K=0$) transitions, respectively, with the H_3 in its ground vibrational level (ν_0). As also noted in the previous study,[46] the incident beam contains $2p\ ^2A_2''$ ($N=K=0$) metastables with vibrational excitation in the symmetric stretch (ν_1) or the degenerate (bending) mode (ν_2). Since the equilibrium distance of the Rydberg levels does not change appreciably with the principal quantum number, the Franck–Condon matrix is expected to be almost diagonal. The smaller peaks in Fig. 1 at 17 211.1 cm^{-1} and 16 651.9 cm^{-1} can be assigned to transitions between symmetric stretch excited levels: $3d\ ^2E''\ \nu_1$ ($N=1$, $G=0$, $R=1$) $\leftarrow 2p\ ^2A_2''\ \nu_1$ ($N=K=0$) and $3s\ ^2A_1''\ \nu_1$ ($N=1$, $K=0$) $\leftarrow 2p\ ^2A_2''\ \nu_1$ ($N=K=0$), respectively. The predicted values of these transition frequencies, derived from a combination of the ν_0 transition frequencies[20,23] with the symmetric stretch excitation frequencies (ν_1) of the states as measured by Lembo and Helm[37] and by Lembo *et al.*,[38] are included with the present measurements in Table I. This table also summarizes the results of a high-resolution experiment performed by Bjerre *et al.*[47] in which the fine-structure splitting of the $3s$ and $3d$ levels was resolved. Our results agree with those of other investigations within the uncertainty of our wavelength determination, 0.3 cm^{-1}. The peaks at 17 195.8 cm^{-1} and 16 665.7 cm^{-1} correspond to transitions between vibrationally degenerate mode (ν_2) levels: $3d\ ^2E''\ \nu_2$ ($N=1$, $G=0$, $R=1$)$\leftarrow 2p\ ^2A_2''\ \nu_2$ ($N=K=0$) and $3s\ ^2A_1'\ \nu_2$ ($N=1$, $K=0$)$\leftarrow 2p\ ^2A_2''\ \nu_2$ ($N=K=0$), respectively.

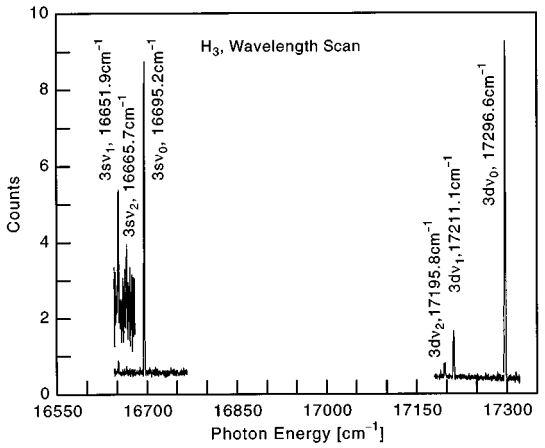

FIG. 1. Flux of $H+H_2$ photofragments with kinetic energy releases in the range $3.5\ \text{eV} \leqslant W \leqslant 8\ \text{eV}$ recorded as a function of the laser photon energy. The count rate was normalized to the metastable flux during this scan so the relative sizes of the photofragment peaks are not exactly proportional to the H_3 transition intensities.

The distributions of the fragment mass ratio Z [see Eq. (2)] were examined for the decay of the metastable $2p\ ^2A_2''$ ($N=K=0$) state as well as for photofragments from the $3s\ ^2A_1'$ ($N=1$, $K=0$) and $3d\ ^2E''$ ($N=1$, $G=0$, $R=1$) states. For each of these states, strong peaks are observed at $Z=0.5$ and $Z=2$ which are due to $H+H_2$ fragment pairs, where the heavier (H_2) fragment hits on side 1 or side 2 of the detector, respectively. Additionally, a broad, weak feature also appears in the distributions, extending from $Z=0.25$ to $Z=2.5$ with a maximum around $Z=1.0$. This feature, which is nearly absent for the $2p\ ^2A_2''$ decay and is strongest for the $3s\ ^2A_1'$ photodissociation, is indicative of a three-body dissociation of the H_3 level into H+H+H, as will be described elsewhere.[53] For the data reported here, only those events with $0.4 \leqslant Z \leqslant 0.6$ or $1.67 \leqslant Z \leqslant 2.5$ were accepted. This essentially restricts the observations to $H+H_2$ dissociation products, although a small fraction of the three-body dissociation products will also be detected. The effects of these latter products will be noted as they occur in the data.

Figure 2 shows multichannel spectra of the kinetic en-

TABLE I. Observed energies of vibrationally diagonal transitions from the H_3 $2p\ ^2A_2''$ ($N=K=0$) level to the $3s\ ^2A_1'$ ($N=1$, $K=0$) and $3d\ ^2E''$ ($N=1$, $G=0$, $R=1$) levels. Previous measurements of these transition energies are also given. The present measurements have an accuracy of ± 0.3 cm^{-1}. Vibrational spacings between the upper state levels, derived from the present transition energies and the vibrational spacings of the $2p\ ^2A_2''$ state ($\nu_1=3255.34\pm0.03$, $\nu_2=2618.34\pm0.03$) of Ref. 59, are given in the last column. All units are cm^{-1}.

Upper state	Vibrational excitation[a]	This work	Other work	Reference 47	Vibrational energy
$3s\ ^2A_1'$ ($N=1$, $K=0$)	ν_0	16 695.2	16 694.972[b]	16 694.992	
	ν_1	16 651.9	16 651.7[c]		3212.1
	ν_2	16 665.7			2588.8
$3d\ ^2E''$ ($N=1$, $G=0$, $R=1$)	ν_0	17 296.6	17 296.982[d]	17 296.384 ($J=1/2$)	
				17 296.414 ($J=3/2$)	
	ν_1	17 211.1	17 210.0[e]	17 210.857 ($J=1/2$)	3169.9
				17 210.892 ($J=3/2$)	
	ν_2	17 195.8			2517.5

[a]ν_0: vibrational ground state, ν_1: one quantum of symmetric stretch mode excited, ν_2: one quantum of degenerate mode excited.
[b]Reference 20.
[c]Reference 20 transition for the vibrational ground state combined with the ν_1 energies for the upper (Ref. 37) and lower (Ref. 38) states.
[d]Reference 23.
[e]Reference 23 transition for the vibrational ground states combined with the ν_1 energies for the upper (Ref. 37) and lower (Ref. 38) states.

ergy release produced by the fragmentation of 3 keV H_3 into $H+H_2$ pairs for three processes. Spectrum a in Fig. 2 was taken with the laser turned off. Spectrum b in Fig. 2 was recorded with the intracavity dye laser pumping the $3s\ ^2A_1'$ ν_0 ($N=1$, $K=0$)$\leftarrow 2p\ ^2A_2''$ ν_0 ($N=1$, $K=0$) transition at 16 695.2 cm^{-1}. Spectrum c of Fig. 2 was recorded with the intracavity dye laser tuned to the $3d\ ^2E''$ ν_0 ($N=1$, $G=0$, $R=1$)$\leftarrow 2p\ ^2A_2''$ ν_0 ($N=1$, $K=0$) transition at 17 296.6 cm^{-1}. The features of spectra a–c in Fig. 2 can be understood qualitatively as a combination of various radiative and nonradiative decay mechanisms of the H_3 states. Figure 3 shows a diagram of the possible decay channels. The transition rates between the levels connected by optically allowed transitions in Fig. 3 are calculated from the theoretical transition moments of King and Morokuma,[15] which are in close agreement with those of Petsalakis *et al.*[19]

The $2p\ ^2A_2''$ ($N=K=0$) metastables decay with a lifetime of about 640 ns.[34] Fragment pairs from the spontaneous dissociation of this level in the region between the slit and the beam flag are accessible to the detector and produce the

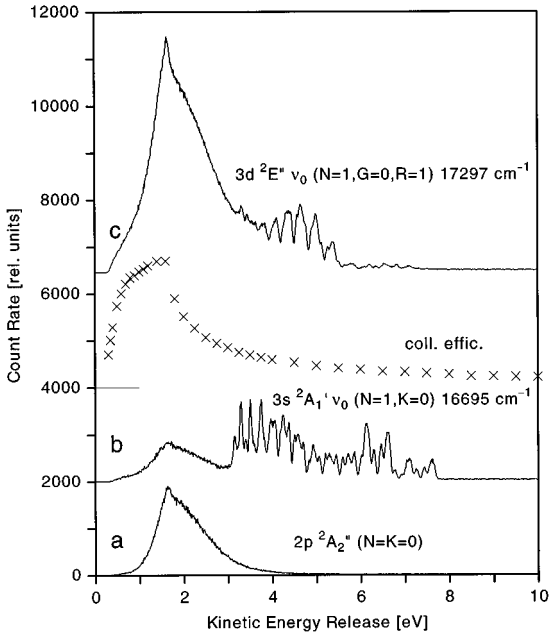

FIG. 2. Uncorrected fragment kinetic energy release spectra produced by the dissociation of 3 keV H_3 molecules under three conditions. a: No laser, or laser tuned away from resonance: spontaneous decay of the metastable $2p\ ^2A_2''$ ($N=K=0$) level. b: Laser tuned to the $3s\ ^2A_1'$ ν_0 ($N=1$, $K=0$)$\leftarrow 2p\ ^2A_2''$ ν_0 ($N=K=0$) transition at 16 695 cm^{-1}. c: Laser tuned to the $3d\ ^2E''$ ν_0 ($N=1$, $G=0$, $R=1$)$\leftarrow 2p\ ^2A_2''$ ν_0 ($N=K=0$) transition at 17 296 cm^{-1}. The crosses in the figure show the variation in apparatus collection efficiency with fragment energy release for photofragments produced from 3 keV H_3 with an angular distribution defined by the asymmetry parameter $\beta=0$. The form of this fragment energy dependence is also typical of other angular distributions.

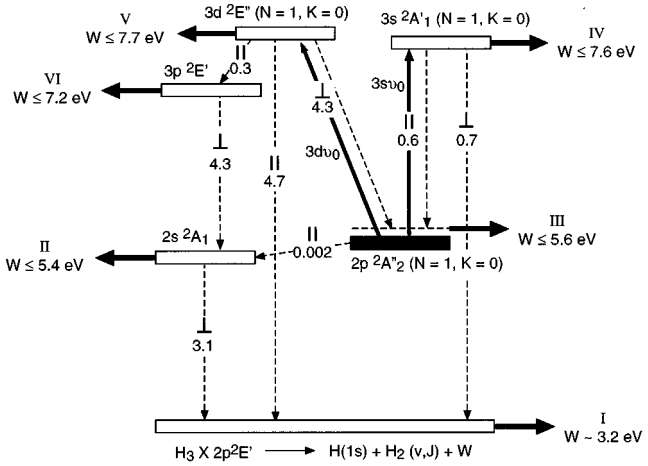

FIG. 3. Schematic diagram of the radiative and predissociative decay mechanisms of the $n=2,3$ Rydberg levels of the H_3 molecule. The radiative decay channels are indicated by broken lines along with their transition rates in 10^7 s^{-1} calculated (see Ref. 25) from the theoretical transition moments of Ref. 15. Predissociative decay pathways into $H+H_2$ fragment pairs are marked by solid horizontal arrows labeled with the maximum kinetic energy release. These energies are relative to $H+H_2$ ($v=0$, $J=0$). For reference, the lowest energy level of H_3^+ lies at 9.227 eV on this scale.

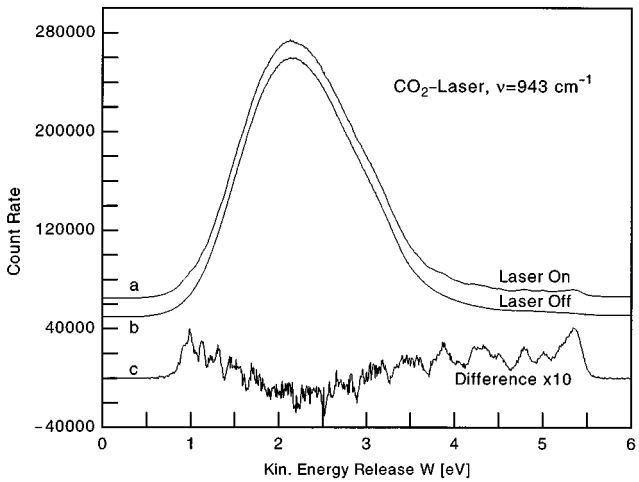

FIG. 4. Kinetic energy release spectrum produced by stimulated emission pumping of the H_3 $2p\ ^2A_2''$ ν_0 ($N=K=0$)$\rightarrow 2s\ ^2A_1'$ ν_0 ($N=1$, $K=0$) transition by a single-mode CW CO_2 laser. The laser polarization was parallel to the metastable beam axis and the primary beam energy was 6 keV. The laser was chopped and curves a and b represent laser-on and laser-off spectra, respectively. The difference spectrum c is magnified by a factor of 10.

broad distribution of kinetic energy releases between 0.5 and 5.5 eV in the laser-off spectrum (a in Fig. 2). Although the H_2 products of this decay are produced in discrete rovibrational levels, the kinetic energy release spectrum is broadened into its continuum appearance by the fact that the dissociations can take place over a 10 cm region. This uncertainty in the value of L_0 in Eq. (4) for a given spontaneous dissociation fragment pair produces an uncertainty in the calculation of the kinetic energy release W, viz. $\Delta W/W \sim 2\Delta L_0/L_0 = 0.095$, which is a factor of 21 larger than the resolution for photodissociation products.

The relatively short, 640 ns, lifetime for the $2p\ ^2A_2''$ ($N=K=0$) metastable level is unusual in that direct coupling to the $\tilde{X}\ 2p\ ^2E'$ continuum is not allowed. Radiative decay into the rapidly predissociated $2s\ ^2A_1'$ ($N=1$, $K=0$) level is one possible decay channel, but the calculated transition rate for this infrared emission (process II in Fig. 3) is two orders of magnitude too slow to explain the lifetime. Similarly, spin-orbit coupling of $2p\ ^2A_2''$ ($N=K=0$) to the $\tilde{X}\ 2p\ ^2E'$ ground state is estimated to account for only about 10% of the observed decay rate.[34,47] Bordas *et al.*[34] have suggested that radiation from this level into asymmetric vibrational modes in the $\tilde{X}\ 2p\ ^2E'$ may be the primary reason for its short lifetime. The present experiments do not directly probe the lifetime of the $2p\ ^2A_2''$ ($N=K=0$), although they do examine the fragment energy distribution produced by predissociation of the $2s\ ^2A_1'$ ($N=1$, $K=0$) level, as will be discussed further. Within the context of the present experiments, the primary interest in the spontaneous decay is twofold: (1) its fragment flux provides a convenient method for monitoring the H_3 beam flux, which is otherwise too small to measure accurately and (2) the spontaneous dissociation fragments obscure a significant range of energies in the photofragment kinetic energy release spectrum and this cannot be eliminated by simply chopping the laser, as will be discussed in detail in the next section.

The fragment kinetic energy release distribution produced by exciting into the $3s\ ^2A_1'$ ($N=1$, $K=0$) level (b in Fig. 2) shows sharp structures between 3 and 8 eV which are due to the predissociation of this level by vibronic or rotational coupling to the repulsive $\tilde{X}\ 2p\ ^2E'$ ground state potential energy surface (process IV in Fig. 3). The 7.633 eV potential energy of this upper state level above the $H+H_2(v=0,J=0)$ dissociation limit[46] may partition only between fragment kinetic energy and the discrete potential energies of the rovibrational levels in the $X^1\Sigma_g^+$ state of the $H_2(v,J)$ fragment. Thus the fragment kinetic energy can assume only discrete values and these appear as the sharp structures in the kinetic energy release spectrum. Predissociation of the $3s\ ^2A_1'$ ($N=1$, $K=0$) level competes with radiative decay into rotationally excited $2p\ ^2A_2''$ levels (process III in Fig. 3) and radiation into the $\tilde{X}\ 2p\ ^2E'$ ground state (process I in Fig. 3). Lifetime studies by Figger *et al.*[25] indicate a $3s\ ^2A_1'$ ($N=1$, $K=0$) lifetime shorter than 4 ns. A lower limit of 0.8 ns for the $3s\ ^2A_1'$ ($N=1$, $K=0$) lifetime was derived from a study of the absorption lineshape by Bjerre *et al.*[47] This puts the total decay rate of the $3s\ ^2A_1'$ ($N=1$, $K=0$) state within the range of 1.3×10^9 s^{-1} and 2.5×10^8 s^{-1}, and shows that nonradiative decay mechanisms dominate the radiative processes, which have transition rates of order 10^7 s^{-1}. The feature in the 0.5–3 eV range of spectrum b in Fig. 2 is actually smaller than that in the laser-off spectrum (a Fig. 2) which shows clearly that the metastable beam is appreciably depleted by the photoexcitation process.

A strong radiative transition ($A=11\times10^7$ s^{-1}) connects the $3d\ ^2E''$ state with the repulsive $\tilde{X}\ 2p\ ^2E'$ ground state surface in a bound-free transition (process I in Fig. 3). The total energy of the upper level is partitioned among the photon energy, the internal excitation of the H_2 fragment, and the kinetic energy release. Since the energy of the radiated photon can assume a continuous range of values, the released kinetic energy is also continuous. This process generates the broad feature in the $0.5 \leqslant W \leqslant 3$ eV range of spectrum c in Fig. 2, which is much more intense than the very similar feature due to spontaneous dissociation in the laser-off spectrum. The structures at $3.2 \leqslant W \leqslant 7.7$ eV in kinetic energy release spectrum b of Fig. 2 are due to direct predissociation (process V in Fig. 3). A weak radiative decay ($A=0.4\times10^7$ s^{-1}) can populate the $3p\ ^2E'$ state, which could either predissociate or radiate into the $2s\ ^2A_1'$ state

The energy difference between the metastable $2p\ ^2A_2''$ ($N=K=0$) level and the lowest Rydberg level $2s\ ^2A_1'$ ($N=1$, $K=0$) is found to be 898 cm^{-1} by combination of the available spectroscopic data.[20,21,23] The $2s$ state is lifetime broadened due to rapid predissociation by vibrational coupling with the repulsive $\tilde{X}\ 2p\ ^2E'$ ground state.[20] The 30 cm^{-1} natural linewidth of transitions connecting this state allows us to stimulate the $2p\ ^2A_2''$ ($N=K=0$)$\rightarrow 2s\ ^2A_1'$ ($N=1$, $K=0$) transition using the 10.6 μm (943 cm^{-1}) radiation of a CO_2 laser. Spectra a and b in Fig. 4 show the kinetic energy release distributions observed with the CO_2 laser on and off respectively. This particular experiment was per-

formed at a primary beam energy $E_0=6$ keV. In addition, a substantial length of the H_3 beam is irradiated by the triple-pass arrangement of the CO_2 laser beam, which degrades the fragment kinetic energy resolution. The energy separation of 5.563 eV between the H_3 $2p\ ^2A_2''$ ($N=K=0$) level and the $H+H_2\ ^1\Sigma_g^+$ ($v=0$, $J=0$) dissociation limit[46] places the H_3 $2s\ ^2A_1'$ ($N=1$, $K=0$) level at 5.451 eV. However, our off-resonance pumping prepares the molecules at a total energy lower than this, viz. 5.446 eV. Structure in the KER spectrum due to vibrational and rotational excitation in the H_2 $^1\Sigma_g^+(v,J)$ fragment appear just on top of the kinetic energy release produced by the metastable decay (b in Fig. 4). Consequently, the data had to be accumulated over a period of 30 hours in order to achieve a reasonable statistical accuracy of the difference spectrum c in Fig. 4, which is amplified by a factor of 10 for clarity. The negative values around 2.5 eV indicate depletion of the metastable beam by the photofragmentation process which will be discussed in the next section.

The objectives of a quantitative data analysis are threefold: (1) separation of the various fragmentation channels: spontaneous dissociation, predissociation, and radiative dissociation; (2) estimation of branching ratios between radiative decay and predissociation; and (3) determination of rotational and vibrational populations of the $H_2(v,J)$ fragment produced by direct predissociation. For a meaningful deconvolution of the experimental spectra, it is required to determine the collection efficiency and the apparatus line shape at any desired kinetic energy release. For a single kinetic energy release, we calculate the apparatus function by a Monte Carlo simulation of the fragment trajectories within the apparatus, taking into account the energy, energy spread, width, and angular divergence of the primary beam, the dimensions and positions of the slit, beam flag, and detector, the uncertainty of the time and position measurement, the lifetime of the molecule (for lifetimes$>$2 ns), and the angular distribution of the fragments. The distribution of the fragment ejection angle Θ with respect to the laser polarization in the c.m. frame is implemented in the Monte Carlo program using the formula

$$I(\Theta)=\frac{1}{4\pi}\left[1+\beta P_2(\cos\Theta)\right], \tag{5}$$

where $P_2(\cos\Theta)=\frac{1}{2}(3\cos^2\Theta-1)$ is the second Legendre polynomial.[54,55] Depending on the alignment parameter β, the distribution varies smoothly from $\sin^2\Theta$ through isotropic to $\cos^2\Theta$ for $\beta=-1\rightarrow0\rightarrow2$, respectively. In order to be useful for the determination of the collection efficiency, the simulation program has to perform a transformation of the angular distribution with respect to the laser polarization into a distribution with respect to the metastable beam direction $I(\theta)$ [see Eq. (3)].

The angular distribution of the axis of a symmetric top following absorption of linearly polarized light is well known.[54] In the case of the $3s\ ^2A_1'$ ($N=1$, $K=0$)$\leftarrow 2p\ ^2A_2''$ ($N=K=0$) transition, the change of dipole moment is parallel to the figure axis (parallel transition) and the resulting

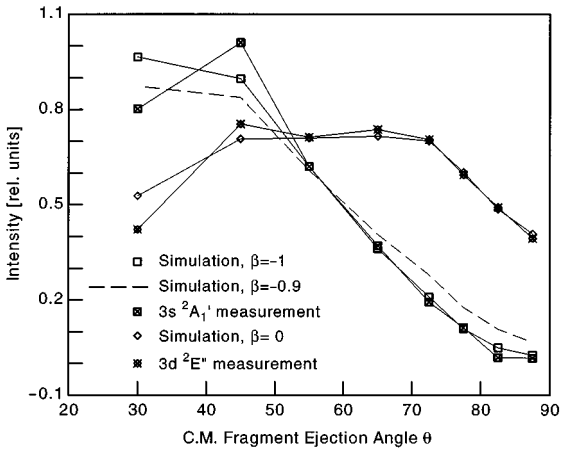

FIG. 5. Distributions of the fragment ejection angle θ with respect to the metastable beam axis for predissociative decay of the $3s\ ^2A_1'$ ($N=1$, $K=0$) level (crossed boxes) and the $3d\ ^2E''$ ($N=1$, $G=0$, $R=1$) level (crossed diamonds). The laser polarization was perpendicular to the metastable beam. Angular distributions calculated by a Monte Carlo simulation for values of the alignment parameter of $\beta=-1$ (open boxes), $\beta=-0.9$ (dashed line), and $\beta=0$ (diamonds) are included for comparison. The solid lines interconnecting the points are not a fit to the data, but are only a guide for defining the data sets.

value of the alignment parameter is $\beta=2$, which corresponds to a $\cos^2\Theta$ distribution of the top axis with respect to the laser polarization. We expect the fragments to be ejected in the molecular plane which is perpendicular to the top axis. The resulting alignment parameter of the fragment ejection angular distribution is a $\sin^2\Theta$ distribution which corresponds to $\beta=-1$. In contrast, the transition from the $2p\ ^2A_2''$ to the degenerate $3d\ ^2E''$ state is a perpendicular transition. The dipole moment is contained in the plane of the molecule. All molecular orientations with the top axis perpendicular to a specific orientation of the dipole moment are equivalent. The fragments are expected to be ejected in the molecular plane with an isotropic distribution around the top axis. Therefore, we expect an isotropic distribution of the fragment ejection angle ($\beta=0$). Since the angular distribution of the fragments influences critically the collection efficiency, empirical tests are required for both electronic transitions. In Fig. 5, measured distributions of the fragment ejection angle with respect to the metastable beam axis $I(\theta)$ of photofragments in the 3–3.5 eV range from the $3s\ ^2A_1'$ state (crossed boxes) and the $3d\ ^2E''$ state (crossed diamonds) are presented along with the results of Monte Carlo simulations for $\beta=-1$ (boxes), $\beta=-0.9$ (dashed line), and $\beta=0$ (diamonds). The results show clearly that the angular distribution of the photofragments can be represented by an alignment parameter of $\beta=-1$ for the $3s\ ^2A_1'$ state and by $\beta=0$ for the $3d\ ^2E''$ state.

The crosses in Fig. 2 show the result of a Monte Carlo simulation of the detector collection efficiency for $H+H_2$ photofragment pairs in the case of 3 keV primary beam energy and an isotropic angular distribution. A 0.4 eV minimum kinetic energy release is required for a pair of fragments, ejected perpendicular to the beam, to each hit a sensitive area of the detector. With increasing energy release,

the collection efficiency increases due to the increase in effective detector solid angle, reaches a maximum at about 1.7 eV, where the lighter of the perpendicularly/ejected fragments impacts just at the outer boundary of the detector, and decreases with still higher energy releases as an increasingly large fraction of the fragments exceed the maximum dimension of the detector. The cut-on and falloff energies depend on the primary beam energy, the ratio of the fragment masses, and the detector geometry, and shift to higher energies with increasing primary beam energy. The structures around 2 eV in the laser-on as well as the laser-off spectra in Fig. 2 are due to the variation of the collection efficiency. We performed systematic tests of the kinetic energy release distributions obtained at different beam energies, applying the detector collection efficiencies calculated for the appropriate conditions, and achieved uniform results for the corrected spectra.

B. Quantitative data analysis

1. The $3d\ ^2E''$ level

By measuring the photofragment flux versus the laser power we find that the transition between the $2p\ ^2A_2''\ \nu_0$ $(N=K=0)$ to the $3d\ ^2E''\ \nu_0$ $(N=1, G=0, R=1)$ state is well saturated. This is consistent with an estimation of the excitation rate from the calculated transition moments,[15] the intracavity laser power, the laser beam geometry, and the metastable beam velocity. Particle loss mechanisms by predissociation or radiation into states other than the metastable deplete the primary beam. By comparing the flux of photofragments produced by the laser to the flux of incident $2p\ ^2A_2''\ \nu_0$ $(N=K=0)$ molecules implied by the spontaneous dissociation fragments (assuming a 640 ns lifetime[46] of this state), we estimate this depletion to be $>80\%$. The laser-off spectrum would thus have to be scaled by a factor <0.2 before subtracting it from the laser-on spectrum. Since the laser-on spectrum in the 0.5–3 eV range is a factor of 5 larger than the laser-off spectrum, the effect of this subtraction is insignificant; hence we choose not to introduce any correction for the laser-off spectrum.

a. $3d\ ^2E''$ radiative dissociation. Spectrum a in Fig. 6 shows the photofragment spectrum of the $3d\ ^2E''\ \nu_0$ $(N=1, G=0, R=1)$ state after correction of the detector collection efficiency. The spectrum is essentially smooth and bell shaped in the 0–3 eV range and shows a maximum at 2.2 eV. These unstructured photofragments arise from radiative transitions onto the dissociative $\tilde{X}\ 2p\ ^2E'$ potential surface. Above 3.3 eV, structures of the direct predissociation process appear. It is clear from Fig. 6 that photofragments from the radiative dissociation and direct predissociation overlap for kinetic energy releases >3.3 eV.

In order to separate the contributions from the radiative and predissociation processes, we examined this same transition in the D_3 molecule. We observed a strong photofragment feature for the D_3 beam with the laser tuned to 17 333 cm^{-1}, which is close to that expected (17 333.273 cm^{-1}) for the $3d\ ^2E''\ \nu_0$ $(N=1, G=0, R=1) \leftarrow 2p\ ^2A_2''\ \nu_0$ $(N=K=0)$ transition.[23] The photofragment energy release spectrum of this transition is shown by spectrum b in Fig. 6. It exhibits a bell-shaped distribution with a maximum at 2.4 eV. The tail in the 4.3–5.5 eV range shows some structure which can be attributed to predissociation, but this structure is greatly attenuated with respect to that observed for H_3. Figger *et al.*[25] have studied emission of the $3d$ states in the triatomic hydrogen isotopomer series and found a reduction of the lifetime with increasing number of hydrogen atoms. Hence, the heavier species are more stable with respect to predissociation than the lighter ones, which accounts for the smaller predissociation contribution in the D_3. As a result, the kinetic energy release spectrum from D_3 can be used as a template for the radiative component in the H_3 spectrum following two small corrections. First, account must be taken of the difference in the vibrational wave functions of the two species which, through the Franck–Condon principle, will yield different widths for their radiative features. For a harmonic oscillator, these should scale as $m^{-1/4}$, which yields a ratio of 1.18 for D_3/H_3. Second, the equilibrium internuclear separations of the $3d$ level are slightly different ($r_0=0.8821$ Å in H_3, $r_0=0.8778$ Å in D_3),[23] which should produce a small shift in the maximum of the radiative peak for the two species. Spectrum c in Fig. 6 was generated from the deuterium measurement (b in Fig. 6) by cutting off the tail above 4.3 eV, expanding the W scale by a factor of 1.15 and recentering the peak. In the 0.5–3.2 eV range, curve c in Fig. 6 is actually falling on top of spectrum a and can be used as a template for the radiative contribution in the energy region where the kinetic energy releases from the radiative and predissociative processes overlap. From the integrals over curves a and c in Fig. 6, we estimate that the radiative transition into the $\tilde{X}\ 2p\ ^2E'$ ground state constitutes 60% of the total flux of $H+H_2$ photofragment pairs.

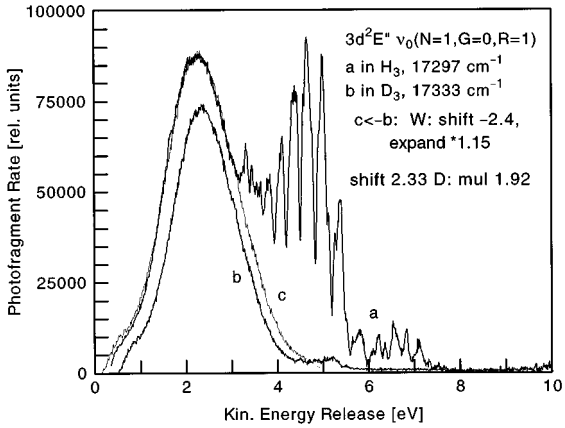

FIG. 6. Photofragment kinetic energy release spectrum produced by excitation to the $3d\ ^2E''\ \nu_0$ $(N=1, G=0, R=1)$ level, excited in H_3 at 17 297 cm^{-1} (curve a) and excited in D_3 at 17 333 cm^{-1} (curve b). The thin line, curve c, was generated from the D_3 spectrum (curve b) by expanding the kinetic energy release scale by a factor of 1.15 and recentering the peak. Curve c is used to define the H_3 fragment energy distribution produced by $3d\ ^2E'' \rightarrow \tilde{X}\ 2p\ ^2E'$ radiative dissociation.

Since we start with an energetically well-defined state and know the kinetic energy of the final products, we can convert the radiative components in the kinetic energy re-

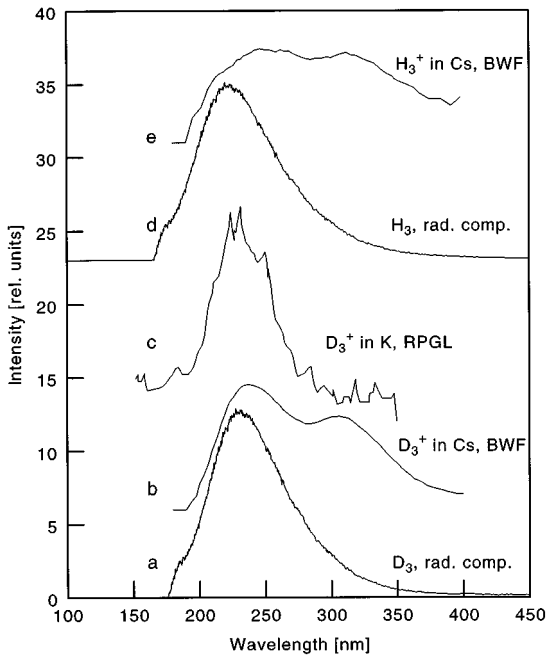

FIG. 7. Curves a and d: transformation of fragment kinetic energy release spectrum produced by the $3d\ ^2E'' \rightarrow \tilde{X}\ 2p\ ^2E'$ transition in H_3 and D_3 into a photon emission spectrum, assuming the final states to be $H+H_2$ ($v=0$, $J=0$) and $D+D_2$ ($v=0$, $J=0$), respectively. Curves b and e are the photoemission spectra observed following charge transfer of D_3^+ and H_3^+, respectively, in cesium vapor (Ref. 28). Curve c is the photoemission spectrum observed following charge transfer of D_3^+ in potassium vapor (Ref. 27).

lease spectra into photoemission spectra under the assumption that the amount of internal excitation of the H_2 final state is negligible. Krause *et al.*[49] examined the dissociation dynamics of H_3^* Rydberg states by a three-dimensional wave-packet analysis. For the radiative decay into the repulsive ground state, they find only very little vibrational excitation of the H_2 final product, which justifies the above assumption. The results of the transformation for deuterium and hydrogen are shown as spectra a and d in Fig. 7 respectively. Raksit *et al.*[27] investigated the photoemission spectrum following interaction between fast D_3^+ ions generated in an electron impact source and a potassium beam. A continuous photoemission spectrum in the 190–280 nm range with maximum around 220 nm (spectrum c in Fig. 7) was observed. The position of the maximum and the shape of the measured photoemission spectrum is in extremely close agreement with the results of our conversion procedure. Bruckmeier *et al.*[28] investigated photoemission spectra in the 200–400 nm range following charge transfer of the isotopomer series of triatomic hydrogen in cesium. A duoplasmatron ion source was used and the light was collected at an adjustable distance downstream from the charge transfer cell. The results of Bruckmeier *et al.*[28] for H_3^+ as well as D_3^+ are included as spectra b and e in Fig. 7 and show two maxima, respectively. The first one around 230 nm coincides with the maximum in our distribution and with the results of the Raksit *et al.*[27] Both measurements[27,28] monitor the light emitted immediately or shortly after charge transfer. The electronic as well as the vibrational excitation of the upper state are not well defined since the charge transfer process can populate all members of the Rydberg series, although the near-resonant product channels should be most highly populated. Based on the strong transition moment between the $3d$ and the $\tilde{X}\ 2p\ ^2E'$ levels[15] and on the fact that the decay of the $2s$ and $3s$ levels is dominated by fast predissociation, it is generally believed that the continuous features in the photoemission spectra are mainly due to the $3d\ ^2E'' \rightarrow \tilde{X}\ 2p\ ^2E'$ bound-free transition. The existence of a second maximum in the results of Bruckmeier *et al.*[28] was attributed to transitions into the upper sheet of the ground state potential energy surface. In order to understand the second maximum around 320 nm in the measurement of Bruckmeier *et al.*[28] in a way consistent with our observation, we would have to assume that dissociation on the upper sheet produces an average internal energy in the H_2 of 1 eV, whereas dissociation on the lower sheet produces little or no internal energy in the H_2 product. Alternatively, if dissociation on the upper sheet was to produce H+H+H products, the 320 nm maximum would not appear in the transformed kinetic energy spectrum, which refers explicitly to $H+H_2$ products. However, dissociation into three atoms is not energetically accessible from the ground vibrational levels of the $n=3$ Rydberg states following the emission of a 320 nm photon. Rather, the emitting state would have to be an $n=3$ Rydberg with at least two quanta of vibrational excitation, or an $n=4$ Rydberg state. Datz *et al.*[56] have found that the fraction of three-body products produced in the dissociative recombination of H_3^+ increased with increasing H_3^+ vibrational excitation. Similarly, Peterson *et al.*[57] have noted that charge transfer neutralization of H_3^+ or D_3^+ in Cs (to form H_3^* or D_3^*) yields a significantly larger fraction of three-body dissociation products when these beams were produced by a Colutron ion source, than when the beams were produced by a hollow-cathode discharge. Since even greater internal excitation can be imparted to the ions in the plasma arc of a duoplasmatron, the possibility that the 320 nm continuum arises from highly excited H_3^* must also be considered, particularly in light of the fact that this continuum was not observed by Raksit *et al.*[27] On the other hand, Bruckmeier *et al.*[28] found comparable rates for the temporal decay of the emission over each of the two continua, which would be difficult to achieve if the 320 nm feature arose solely from highly excited H_3^* levels.

Radiation of the $3d\ ^2E''$ ($N'=1$, $G'=0$, $R'=1$) level is also permitted into the bound $2p\ ^2A_2''$ state. Selection rules[23] would allow both $\Delta N=\pm 1$ transitions, i.e., production of the initial metastable level $2p\ ^2A_2''$ ($N=K=0$) and of the predissociated $2p\ ^2A_2''$ ($N=2$, $K=0$) level. This latter level has a lifetime[20,22] of 13 ps in H_3 and its predissociation should yield structured kinetic energy releases between 1.1 and 5.6 eV. However, there is clearly no evidence for this process in the photofragment spectrum of the $3d\ ^2E''$ ($N'=1$, $G'=0$, $R'=1$) state in D_3 (spectrum b in Fig. 6), despite the fact that the transition rates for radiative decay into the $2p\ ^2A_2''$ and the $\tilde{X}\ 2p\ ^2E'$ states are predicted to be of comparable size.[15] This is consistent with the fact that the calculated intensity for this P-branch transition is very small;[23] hence negligible

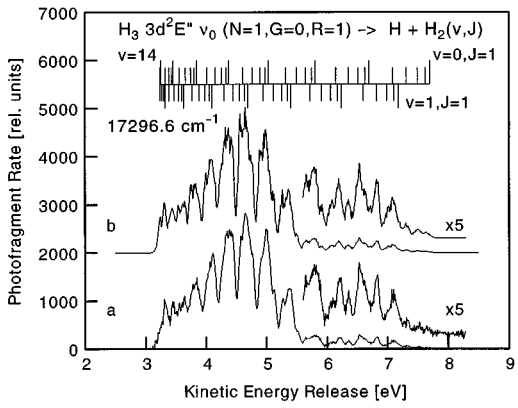

FIG. 8. Predissociation of the H_3 $3d\ ^2E''$ ν_0 ($N=1$, $G=0$, $R=1$) level into a hydrogen atom H($1s$) and a rotationally and vibrationally excited hydrogen molecule H_2 $^1\Sigma_g^+(v,J)$. Curve a is the difference between spectra a and c of Fig. 6. The structures can be assigned to the production of specific H_2 rovibrational levels, as indicated by the tick spectrum. Curve b is a fit to the measurement by a weighted sum of apparatus functions calculated for the individual H_2 rovibrational levels by a Monte Carlo simulation. The weight factors (not shown) correspond to the relative populations in the H_2 (v,J) levels.

production of the rotationally excited level is expected. This simplifies the evaluation of the $3d\ ^2E''$ predissociative component in Fig. 6.

b. $3d\ ^2E''$ *predissociation.* Spectrum a in Fig. 8 shows the photofragment kinetic energy release of the $3d\ ^2E''$ ν_0 ($N=1$, $G=0$, $R=1$) level after subtraction of the radiative contribution (spectrum c in Fig. 6). The tick spectrum indicates the kinetic energy releases expected from direct predissociation into $H+H_2$ $^1\Sigma_g^+(v,J)$ fragment pairs. For clarity of presentation, ticks belonging to odd values of vibrational quantum number were drawn negative and the beginning of each rotational progression was marked by a longer tick. The rovibrational energy levels of the H_2 $^1\Sigma_g^+$ state were calculated from the potential curve by Schwartz and LeRoy.[58] The energy of the upper state with respect to the $H+H_2$ $^1\Sigma_g^+$ ($v=0$, $J=0$) dissociation limit was taken from Cosby and Helm.[46] As already discussed, the nuclear spins in the vibrational ground level of the $2p\ ^2A_2''$ ($N=K=0$) state are coupled with $I_{\rm tot}=3/2$.[33] Since the nuclear spin is not expected to reorient during the rapid fragmentation process, we have $I_{\rm total}=1$ in the H_2 fragment and only rotational levels with odd values of the angular momentum J (*ortho* levels) occur in the spectrum. The structures in the experimental spectrum (a in Fig. 8) correspond to the calculated positions. The signal in the 3.3–5.5 eV range is much higher than in the 5.5–7.7 eV range, which indicates a drastic change in the H_2 final state vibrational population around $v=5$. Spectrum b in Fig. 8 is a fit to the measured spectrum by a weighted sum of apparatus functions calculated by the Monte Carlo simulation program at the expected kinetic energy releases.

The $3d\ ^2E''$ ν_0 predissociation structure is unique among the states investigated in the present experiments in that its features are appreciably broadened with respect to the kinetic energy resolution expected for a 0.2 cm laser interaction region. This broadening is due to the comparatively long lifetime of the $3d$ state. Figger *et al.*[25] investigated the lifetime of the $3d$ states in D_3 and H_3 by emission spectroscopy following charge transfer of D_3^+ and H_3^+ in Cs. They found the lifetime in D_3 to be quite independent of the selected spectral range (i.e., the initial rotational level), reporting values between 11.6 and 12.5 ns. The sum of the calculated radiative decay rates from the $3d\ ^2E''$ into the $2p\ ^2A_2''$, $3p\ ^2E'$, and $\tilde{X}$ $2p\ ^2E'$ states as shown in Fig. 3 is 9.3×10^7 s^{-1}. In the case of D_3, the direct predissociation rates are negligible compared to the radiative decay processes and the reciprocal of the calculated transition rates, 10.7 ns, agrees very well with the observed lifetime values. In the case of H_3, the measured lifetimes vary between 3.5 and 11.0 ns depending on the selected wavelength range.[25] Part of this variation is likely due to the overlap of emissions from other states in the measurements. We estimate a lifetime of 8.1 ns for the H_3 $3d\ ^2E''$ ν_0 ($N=1$, $G=0$, $R=1$) level from the calculated 9.3×10^7 s^{-1} radiative decay rate and a predissociation rate which was determined above to be $\frac{2}{3}$ of the $3d\ ^2E''\rightarrow\tilde{X}\ 2p\ ^2E'$ bound-free transition rate of 4.7×10^7 s^{-1}. Over this 8.1 ns lifetime, the 3 keV H_3 molecules travel about 0.4 cm, which is significantly larger than the laser beam diameter. Consequently, we have included this exponential decay of the H_3 $3d\ ^2E''$ ν_0 state in the Monte Carlo simulation of its apparatus functions.

Magnified plots of the measured kinetic energy release spectrum together with the simulations are shown for the 5.5–8 eV range in Fig. 8. It can be seen that the simulation is of high quality even in regions of low fragment intensity. [The weight factors, representing the rovibrational population distribution in the H_2 (v,J) fragments, are shown in Fig. 14(d).]

c. $3d\ ^2E''$ ν_1, ν_2 *dissociation.* The vibrationally excited components in the $2p\ ^2A_2''$ metastable beam allow us to study the fragmentation of the $3d\ ^2E''$ ν_1 ($N=1$, $G=0$, $R=1$) state having one quantum of excitation in the symmetric stretch mode. The decay of vibrational ground state metastables, which represent the majority in the incoming beam, dominates both the laser-on and the laser-off spectra. Consequently, many hours of data collection were required in order to achieve a reasonable statistical accuracy in the photofragment kinetic energy release spectrum. Since the vibrational population in the metastable beam is initially unknown, we selected the scaling factor for subtraction of the laser-off spectrum in such a way that no part of the difference spectrum becomes significantly negative. This procedure is somewhat arbitrary since it relies on the assumption that the kinetic energy release spectra of the vibrational ground and excited level metastables are (essentially) identical. In spectrum a of Fig. 9, a scaling factor of 0.86 for the laser-off spectrum was applied and the spectrum was corrected for detector collection efficiency. Under the assumption that the transition is saturated and the lower level population is effectively depleted, we estimate from the scaling factor that about 14% of the metastables are in a symmetric stretch excited (ν_1) level. Spectrum a in Fig. 9 shows a continuous distribution of kinetic energy releases between 1.0 and 3.5 eV which is attributed to radiative decay into the repulsive $\tilde{X}$

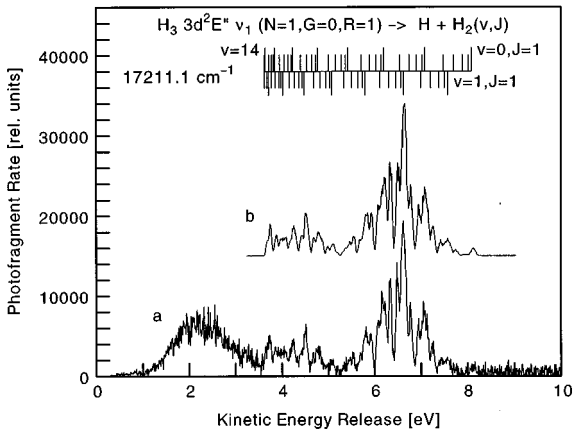

FIG. 9. Spectrum a is the photofragment kinetic energy release spectrum produced by the symmetric-stretch-excited H_3 $3d\ ^2E''\ \nu_1$ ($N=1$, $G=0$, $R=1$) level. The spectrum is corrected for apparatus collection efficiency. Assignment of the structures produced by predissociation into H($1s$) and rovibrationally excited H_2 $^1\Sigma_g^+(v,J)$ fragments is indicated by the tick spectrum. The bell-shaped feature at 1 eV$\leqslant W\leqslant$3.5 eV is produced by $3d\ ^2E''\ \nu_1 \rightarrow \tilde{X}\ 2p\ ^2E'$ radiative dissociation. Spectrum b is a fit to the predissociation products in spectrum a by a weighted sum of apparatus functions calculated for the individual H_2 rovibrational levels by a Monte Carlo simulation.

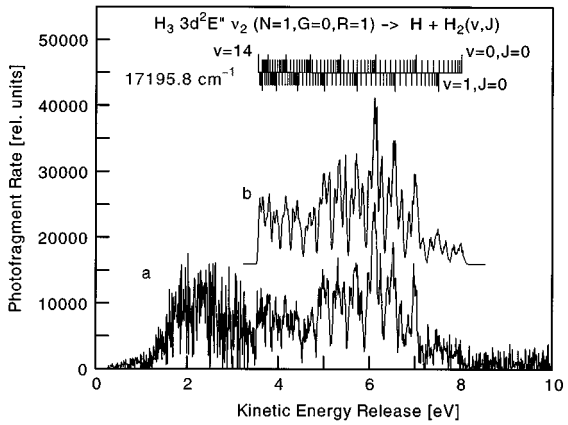

FIG. 10. Spectrum a: photofragment kinetic energy release spectrum of the degenerate-mode-excited H_3 $3d\ ^2E''\ \nu_2$ ($N=1$, $G=0$, $R=1$) level. The spectrum is corrected for apparatus collection efficiency. Assignment of the structures due to predissociation into H($1s$) and rovibrationally excited H_2 $^1\Sigma_g^+(v,J)$ fragments is indicated by the tick spectrum. The feature at 1 eV$\leqslant W\leqslant$3.5 eV is produced by $3d\ ^2E''\ \nu_2 \rightarrow \tilde{X}\ 2p\ ^2E'$ radiative dissociation. Spectrum b is a fit to the predissociation fragments in spectrum a by a weighted sum of apparatus functions calculated for the individual H_2 rovibrational levels by a Monte Carlo simulation.

$2p\ ^2E'$. By integration of the spectrum, we *estimate* a lower limit of 0.37 for the ratio between the radiative component and the total two-particle photofragmentation. This ratio is sensitively affected by the scaling factor for the laser-off spectrum. The pronounced structures between 3.5 and 8.2 eV can be assigned to direct predissociation as indicated by the tick spectrum of the H_2 $^1\Sigma_g^+(v,J)$ fragment rovibrational levels. The symmetric stretch excitation frequency of the $3d\ ^2E''$ ($N=1$, $G=0$, $R=1$) state was measured by Lembo *et al.*[37] to be 3168.4 cm^{-1} and this places the total available energy of the $3d\ ^2E''\ \nu_1$ ($N=1$, $G=0$, $R=1$) at 8.101 eV above the $H+H_2$ $^1\Sigma_g^+$ ($v=0$, $J=0$) limit. Spectrum b in Fig. 9 is the fit to the experimental spectrum. [The corresponding rovibrational distribution of the H_2 (v,J) fragment is shown in Fig. 14(e).]

With the laser tuned to 17 195.8 cm^{-1}, the vibrationally bending excited $3d\ ^2E''\ \nu_2$ ($N=1$, $G=0$, $R=1$) state is prepared. The amount of vibrational-bending-excited metastables in the primary beam is even smaller than the amount of symmetric stretch excited ones. One day of continuous operation of the experiment was required to achieve the result in Fig. 10. A scaling factor of 0.98 for the laser-off spectrum was selected empirically as the highest possible value at which the difference spectrum remains positive. The feature in the 1–3 eV range can be attributed to a radiative transition into the $\tilde{X}\ 2p\ ^2E'$. The ratio between the radiative decay and the total two-particle breakup is *estimated* to be 31%, a value which is sensitively affected by the scaling of the laser-off spectrum. The clear and pronounced structures in the 3.5–8 eV range are due to direct predissociation. We can predict the total energy of the $3d\ ^2E''\ \nu_2$ ($N=1$, $G=0$, $R=1$) to be 8.020 eV from the energy of the $2p\ ^2A_2''\ \nu_0$ ($N=K=0$) level[46] (5.563 eV), the $2p\ ^2A_2''\ \nu_2$ vibrational energy[59] (2618.34 cm^{-1}), and the present transition energy. The experimental spectrum is consistent with this energy. Spectrum b in Fig. 10 is the fit to the experimental spectrum. Note that all rotational levels of the H_2 product must be included in this fit. Due to the angular momentum of the degenerate vibrational mode, the nuclear spin in the H_3 is coupled with $I_{tot}=\frac{1}{2}$; hence dissociation can yield either *ortho* or *para* H_2. [The rovibrational population of the H_2 fragment is shown in Fig. 14(f)]. We observe an average intensity ratio of 2.1:1 between odd and even values of the angular momentum J.

2. The $3s\ ^2A_1'$ level

An investigation of the photofragment flux following excitation of the $3s\ ^2A_1'\ \nu_0$ ($N=1$, $K=0$)$\leftarrow 2p\ ^2A_2''\ \nu_0$ ($N=K=0$) transition indicates that we almost totally deplete the metastable beam by the excitation/predissociation process. This means that the structure in the 0–3 eV range of spectrum b of Fig. 2 is due primarily to photofragments produced by spontaneous radiation of the optically prepared $3s\ ^2A_1'$ level into the repulsive $\tilde{X}\ 2p\ ^2E'$ ground state surface. The fragment angular distribution in the low-energy range is found to be isotropic, which can be understood by the nature of the perpendicular transition between a nondegenerate and a degenerate state. Since the equilibrium internuclear distances of the $3s$ and the $3d$ levels are similar,[23] we used the radiative component of the $3d$ state decay (spectrum c in Fig. 6) as a template for the fragment kinetic energy distribution for this process in the $3s\ ^2A_1'$ state. In the 0.5–1.5 eV range, the spectra of the radiative component and the metastable decay spectrum differ appreciably, which allows an accurate deconvolution of the low-energy part of the $3s$ spectrum. The weight factor for the laser-off spectrum is found to be 0.16. This is consistent with the fraction of vibrationally excited metastables in the primary beam, which

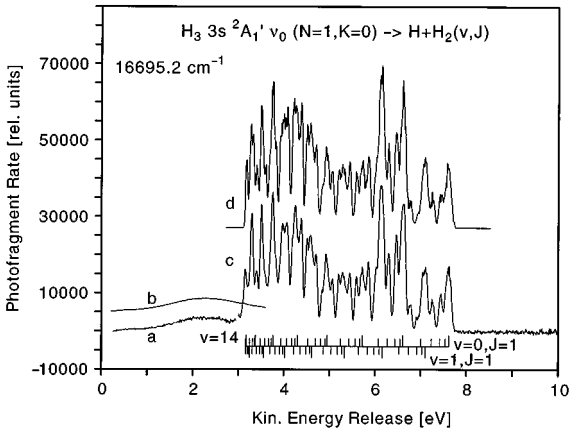

FIG. 11. Spectra a and c: photofragment kinetic energy release spectrum of the vibrational ground state $3s\ ^2A_1'\ \nu_0\ (N=1,\ K=0)$ level of H_3. The structures above 3 eV are due to predissociation into H($1s$) and rovibrationally excited $H_2\ ^1\Sigma_g^+(v,J)$ fragments as indicated by the tick spectrum. The feature below 3 eV is produced by $3s\ ^2A_1'\ \nu_0 \rightarrow \tilde{X}\ 2p\ ^2E'$ radiative dissociation. The apparatus collection efficiency, which depends on the fragment ejection angle with respect to the laser polarization, was corrected separately in the ranges below and above 3 eV using an isotropic distribution ($\beta=0$) for the radiative dissociation fragments (curve a) and a $\sin^2\Theta$ distribution ($\beta=-1$) for the predissociation fragments (curve c). The shape of the $3s\ ^2A_1'\ \nu_0 \rightarrow \tilde{X}\ 2p\ ^2E'$ feature (curve a) is essentially identical to that produced by $3d\ ^2E''\ \nu_2 \rightarrow \tilde{X}\ 2p\ ^2E'$ radiative dissociation. For comparison, spectrum c of Fig. 6 was scaled appropriately and included as curve b in this figure. Spectrum d: the predissociation fragments fitted by a weighted sum of apparatus functions calculated for the individual H_2 rovibrational levels by a Monte Carlo simulation.

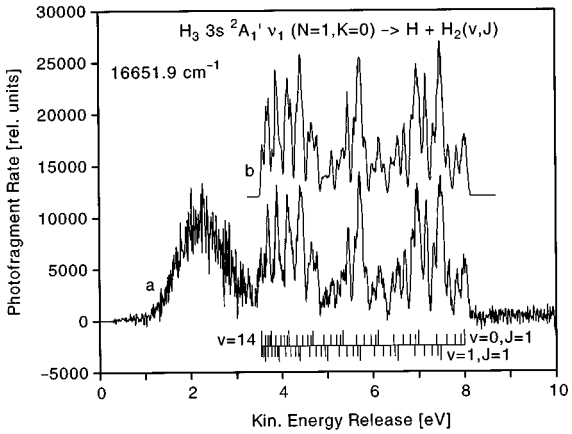

FIG. 12. Spectrum a: photofragment kinetic energy release spectrum of the symmetric-stretch-excited $3s\ ^2A_1'\ \nu_1\ (N=1,\ K=0)$ level of H_3. The apparatus collection efficiency was corrected by a procedure similar to that described in Fig. 11. Assignment of the structures due to predissociation into H($1s$) and rovibrationally excited $H_2\ ^1\Sigma_g^+(v,J)$ fragments is indicated by the tick spectrum. Spectrum b is a fit to the predissociation fragments in spectrum a by a weighted sum of apparatus functions calculated for the individual H_2 rovibrational levels by a Monte Carlo simulation. The feature at 1 eV$\leqslant W \leqslant$3.5 eV arises from $3s\ ^2A_1'\ \nu_1 \rightarrow \tilde{X}\ 2p\ ^2E'$ radiative dissociation.

cannot be depleted at this excitation wavelength. After subtracting the weighted laser-off-spectrum, we corrected the measured spectrum for the apparatus collection efficiency calculated by the Monte Carlo simulation. This was done separately for the range below and above 3 eV since the angular distributions for the radiative and the predissociative process are different. The corrected kinetic energy release distribution is shown by spectrum a in Fig. 11 and its simulation is given by spectrum c. Spectrum b in this figure corresponds to the radiative contribution (spectrum c in Fig. 6) which fits the low-energy part extremely well. We find the ratio between radiative decay and the total two-body predissociation of this level to be 9%.

The structures in the 3–7.7 eV range are due to direct predissociation of the $3s\ ^2A_1'\ (N=1,\ K=0)\ \nu_0$ level and correspond to the expected kinetic energy releases as indicated by the tick spectrum. For low vibrational excitation, the rotational structure is well resolved. The $J=5$, and $J=7$ levels in $v=0$ are separated and it can be seen directly from the spectrum that the $J=6$ level is not populated at all, which justifies the assumption of the nuclear spin conservation during the fragmentation process. Spectrum d in Fig. 11 is a fit to the experimental result by a weighted sum of apparatus functions calculated by a Monte Carlo simulation. [The vibrational and rotational population of the $H_2\ (v,J)$ final product are presented in Fig. 14(a).]

With the laser tuned to 16 651.9 cm^{-1}, we excited the $3s\ ^2A_1'\ \nu_1\ (N=1,\ K=0) \leftarrow 2p\ ^2A_2''\ \nu_1\ (N=K=0)$ transition. As already discussed in the case of the $3d\ \nu_1$ excitation, both the laser-on and laser-off spectra are superimposed by a strong contribution of spontaneous dissociation products from the undepleted vibrational ground state metastable level. Ten hours of continuous data accumulation were required in order to achieve sufficient statistical accuracy in the photofragment kinetic energy spectrum. As an additional complication, the absorption line is weaker and narrower than for the corresponding $3d \leftarrow 2p$ transition, which makes it very difficult to maintain a stable laser frequency on the line for long periods of time. Therefore, the scaling of the laser-off spectrum is somewhat problematic. A scaling factor of 0.95 is found to be the highest possible value that prevents the difference spectrum from becoming significantly negative. In the 0.5–3.3 eV range, a continuous feature appears in the difference spectrum which is attributed to a radiative transition into the repulsive $\tilde{X}\ 2p\ ^2E'$ state. Since the angular distributions for the radiative and the predissociative process are different, as already discussed, the correction of the apparatus collection efficiency using the results of the Monte Carlo simulation was done separately for the range below and above 3.3 eV with values of $\beta=0$ and $\beta=-1$ for the alignment parameter, respectively. The corrected difference spectrum is shown in Fig. 12 (spectrum a). We find a ratio of 0.15 between the continuous contribution and the total two-particle decay. This ratio is by a factor of 2 higher than in the case of the $3s\ ^2A_1'\ (N=1,\ K=0)\ \nu_0$ state, but note that this ratio is extremely sensitive to the scaling of the laser-off spectrum.

The discrete structures at kinetic energy releases between 3.5 and 8.1 eV are due to direct predissociation of the $3s\ ^2A_1'\ \nu_1\ (N=1,\ K=0)$ level. The assignment of the $H_2\ ^1\Sigma_g^+$ final state rotational and vibrational excitation as indicated

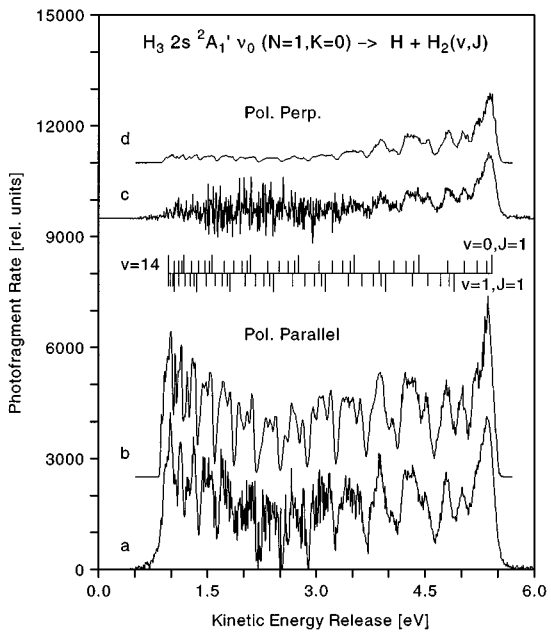

FIG. 13. Spectra a and c: Photofragment kinetic energy release spectrum of the H_3 $2s\ ^2A_1'$ ($N=1$, $K=0$) level with the laser polarization oriented parallel (a) and perpendicular (c) to the metastable beam. The assignment of the structures due to direct predissociation into H($1s$) and rovibrationally excited H_2 $^1\Sigma_g^+(v,J)$ fragments is indicated by the tick spectrum. Spectra b and d are fits to the measured spectra by weighted sums of apparatus functions calculated for the individual H_2 rovibrational levels by a Monte Carlo simulation. The two simulations reflect identical populations in the $H_2(v,J)$ fragments.

by the tick spectrum in Fig. 12 is based on the 7.633 eV energy of the $3s\ ^2A_1'$ ν_0 ($N=1$, $K=0$) level above the $H+H_2$ ($v=0$, $J=0$) dissociation limit[46] and the 3212.1 cm^{-1} symmetric stretch frequency measured by Lembo *et al.*[37] These place the total available energy of the $3s\ ^2A_1'$ ν_1 ($N=1$, $K=0$) level at 8.031 eV. Spectrum b in Fig. 12 is the fit to the experimental spectrum. [The corresponding rovibrational distribution of the H_2 (v,J) fragment is shown in Fig. 14(b).]

3. The $2s\ ^2A_1'$ level

As already discussed above, the $2p\ ^2A_2''$ ν_0 ($N=K=0$)$\rightarrow 2s\ ^2A_1'$ ν_0 ($N=1$, $K=0$) transition was pumped by a CO_2 laser. The design of the CO_2 laser allowed us to rotate the polarization and to perform separate measurements with the electric vector of the laser beam oriented either parallel or perpendicular to the metastable beam axis. The results are shown as spectra a and c in Fig. 13. As discussed above, the laser-off spectra have to be scaled appropriately in order to take a depletion of the metastable beam into account. The scaling factors were adjusted in such a way that no part of the difference spectra was significantly negative. The systematic uncertainty induced by this procedure is highest around 2 eV at the maximum of the metastable decay spectrum. Scaling factors of 0.987 and 0.993 were applied for the measurements with polarization parallel (a in Fig. 13) and perpendicular (b in Fig. 13) to the metastable beam respectively. These values are consistent with the amount of depletion estimated from the calculated transition moments,[15,19] laser power, beam diameter, and metastable beam velocity. No contribution from radiative decay of the $2s\ ^2A_1'$ state onto the repulsive $\tilde{X}\ 2p\ ^2E'$ ground state potential surface appears in the kinetic energy release spectrum and none is expected. The radiative transition rate for that process is estimated to be $A=0.7\times10^7\ s^{-1}$ from the transition moments of King and Morokuma,[15] which is six orders of magnitude smaller than the $A=5.6\times10^{12}\ s^{-1}$ total decay rate of the $2s\ ^2A_1'$ state estimated from the 30 cm^{-1} lifetime broadening that has been observed for transitions into this state.[20] The structures in the kinetic energy release spectrum are due to the discrete kinetic energy releases upon breakup of the initial $2s\ ^2A_1'$ ν_0 ($N=1$, $K=0$) state into H($1s$) and H_2 $^1\Sigma_g^+(v,J)$ fragment pairs as indicated by the ticks in Fig. 13.

The vibrational spacing of the $2s\ ^2A_1'$ state in H_3 is unknown. We estimate a value of 3230 cm^{-1} by extrapolation of the spacings for the ns^2A_1' Rydberg series measured by Lembo and Helm.[37] Given the vibrational spacing of 3255.4 cm^{-1} in the $2p\ ^2A_2''$ state,[37,59] we estimate the $2p\ ^2A_2''$ ν_1 ($N=K=0$)$\rightarrow 2s\ ^2A_1'$ ν_1 ($N=1$, $K=0$) transition to occur around 923 cm^{-1}, which would be even closer to the 940 cm^{-1} frequency of the CO_2 laser than the ν_0 transition at 898 cm^{-1} and therefore more easily excited. Alternately, we could estimate a ν_1 vibrational spacing of 3394 cm^{-1} for the $2s\ ^2A_1'$ state of H_3 from that reported[25] for D_3 (2457 ± 10 cm^{-1}). This value would imply a $2p\ ^2A_2''$ ν_1 ($N=K=0$)$\rightarrow 2s\ ^2A_1'$ ν_1 ($N=1$, $K=0$) transition energy of 761 cm^{-1}, which could not be pumped by the CO_2 laser. In any event, the high energy cutoff in the kinetic energy release spectrum of the $2s\ ^2A_1'$ ν_1 ($N=1$, $K=0$) state should appear about 0.3 eV above that of the ν_0 level. Although the ν_1 population in the metastable beam was estimated to constitute about 14% of the total metastable flux, we do not see any signal in the kinetic energy spectrum above the cutoff of the ν_0 level. We therefore assume the contribution of the ν_1 level to be negligible.

The fragment angular distribution should be essentially the same as for the $3s\ ^2A_1'$ ($N=1$, $K=0$)$\leftarrow 2p\ ^2A_1''$ ($N=K=0$) transition, which is described by an alignment parameter of $\beta=-1$. The fragments are ejected preferentially perpendicular to the laser polarization. With the laser polarization parallel the metastable beam axis, the apparatus collection efficiency is enhanced at low kinetic energies which can immediately be seen by comparing spectra a and c in Fig. 13. Each of the experimental spectra was fitted by a weighted sum of apparatus functions, respectively, calculated by the Monte Carlo simulation program (c and d in Fig. 13), which took account of the direction of laser polarization. A single set of weight factors representing the vibrational and rotational populations of the H_2 fragment was suitable to fit both measurements. This set is plotted in Fig. 14(c).

Comparison can be made between the present fragment kinetic energy release distribution (Fig. 13) and the product center-of-mass frame energy distributions observed by Vogler[60] from the dissociative charge transfer of H_3^+ in H_2. The close correspondence of the features in the two spectra

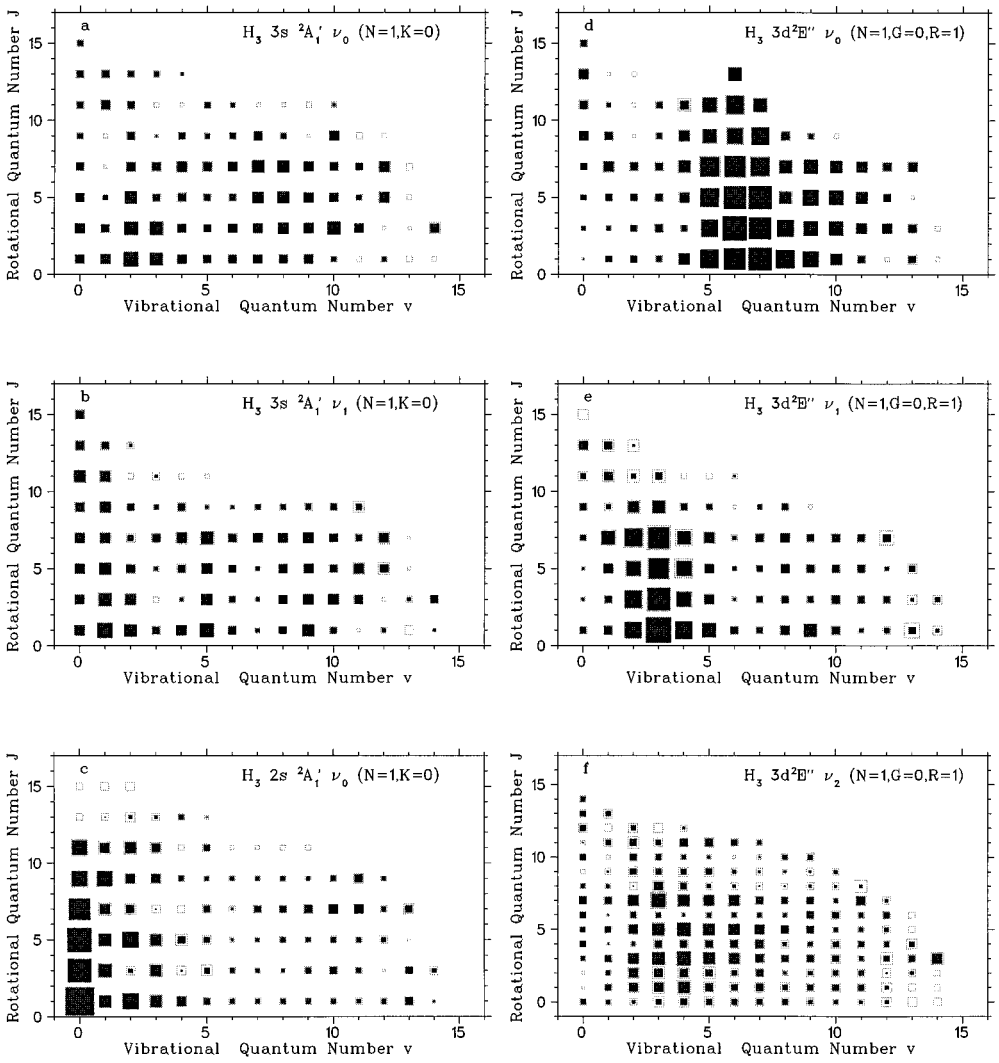

FIG. 14. Rovibrational populations of the product $H_2(v,J)$ fragments produced by predissociation of six H_3 Rydberg levels: (a) $3s\ ^2A_1'$ ν_0 ($N=1$, $K=0$); (b) $3s\ ^2A_1'$ ν_1 ($N=1$, $K=0$); (c) $2s\ ^2A_1'$ ν_0 ($N=1$, $K=0$); (d) $3d\ ^2E''$ ν_0 ($N=1$, $G=0$, $R=1$); (e) $3d\ ^2E''$ ν_1 ($N=1$, $G=0$, $R=1$); and (f) $3d\ ^2E''$ ν_2 ($N=1$, $G=0$, $R=1$). The relative $H_2(v,J)$ populations are denoted by the areas of the solid squares. Error bars are indicated by the open squares surrounding those data points with a relative uncertainty exceeding 15%.

confirm Watson's conclusion[61] that Vogler was observing the predissociation products of the H_3 $2s\ ^2A_1'$ state.

IV. DISCUSSION

A. Rovibrational product distributions

The relative rovibrational populations in the H_2 $^1\Sigma_g^+(v,J)$ fragment resulting from two-body predissociation of the various H_3 states are summarized in Fig. 14. In this figure, the areas of the filled squares are proportional to the relative populations obtained from the fits to the fragment kinetic energy distributions. The sensitivity of the population in a given product level from the nonlinear fit is indicated by the area of the surrounding open square, for those levels where the relative uncertainty exceeds 15%. An additional, systematic uncertainty in the determination of the rovibrational distributions arises generally for higher rotational levels because of their overlap with lower rotational levels of the next higher vibrational state. The problem becomes serious at high vibrational levels, and therefore we progressively restricted the number of rotational levels included in the fit of the higher vibrational levels, as can be seen from the data in Fig. 14.

Since predissociation of a H_3 level represents a single, well-defined potential energy that must be partitioned among translational energy, vibrational energy of the H_2 product, and rotational energy of the H_2 product, one might expect to find a systematic correlation between the vibrational and rotational populations in the experimental H_2 product state distributions. However, an examination of Fig. 14 suggests that such trends, if present at all, are far from obvious. Production of specific $H_2(v,J)$ levels seems almost arbitrary in the predissociation of a given H_3 level, and the $H_2(v,J)$ levels differ widely in their production by different H_3 levels. This large variation in the $H_2(v,J)$ population distribution with electronic state is especially remarkable, since the potential

curves of the Rydberg states are expected to be quite similar to that of the H_3^+ ion core. Indeed, the vibrational spacings of the $2p$, $3s$, and $3d$ states studied here, differ less than 4% from those of H_3^+. Secondly, the $3s$ and $3d$ states lie very close in energy; the difference in their energies being $<1\%$ of their energy above the $H+H_2$ ($v=0$, $J=0$) dissociation asymptote.

The $ns\,^2A_1'$ levels should be predissociated by vibronic coupling to the $\tilde{X}\ 2p\ ^2E'$ ground state surface, with the $2s$ and $3s$ states differing in their Franck–Condon overlap with this predissociating state. This latter effect is believed to be responsible for the large difference in the lifetimes of the $2s$ and $3s$ ground vibrational levels.[43] In the case of the $3s$ $^2A_1'$ ν_0 ($N=1$, $K=0$) level [Fig. 14(a)], population maxima appear at $v=2$, $J=1$, at $v=7$, $J=7$, and at $v=10$, $J=3$. The addition of one quantum of symmetric stretch excitation to the $3s$ $^2A_1'$ ($N=1$, $K=0$) level [Fig. 14(b)] seems to produce a rectangular grid in the product population with intensity maxima at the corners: $v=1,5,9$ and $J=1,7$. In the case of the $2s$ $^2A_1'$ ν_0 ($N=1$, $K=0$) level [Fig. 14(c)], the $J=1$ level of $v=0$ is clearly the most highly populated in the predissociation, with the populations in the other product levels decreasing slowly for higher rotation and very rapidly for higher vibration. A minimum occurs at $v=8$, $J=3$ and a local maximum at $v=10$, $J=7$. Qualitatively viewing the population distributions produced by the $2s$ $^2A_1'$, $3s$ $^2A_1'$ ν_0, and $3s$ $^2A_1'$ ν_1 levels gives the impression that the strong feature at $v=0$ in the $2s$ $^2A_1'$ products moves to $v=2$ in the $3s$ $^2A_1'$ ν_0 products and to $v=5$ in the $3s$ $^2A_1'$ ν_1 products, with new features coming from the boundaries into the picture.

The $3d$ $^2E''$ states are predissociated by rotational coupling to the $\tilde{X}\ 2p\ ^2E'$ ground state. The $H_2(v,J)$ rovibrational population resulting from predissociation of the $3d$ $^2E''$ ν_0 ($N=1$, $G=0$, $R=1$) level [Fig. 14(d)] shows a rather well-defined ridge centered at $v=6$ that descends slowly with increasing J and more rapidly for lower and higher vibrational excitation. The $v=0$, $J=1$ level is not populated at all, but some production is found of higher rotational states of $v=0$. For the $3d$ $^2E''$ level with one quantum of excitation in the symmetric stretch mode [Fig. 14(e)], a ridge similar to that produced by the ground vibrational level [Fig. 14(d)] is found centered at $v=3$. Local maxima also appear at $v=8$, $J=7$ and $v=9$, $J=1$. The $H_2(v,J)$ population distribution produced by predissociation of the $3d$ $^2E''$ ($N=1$, $G=0$, $R=1$) level with one quantum of excitation in the degenerate vibrational mode, ν_2 [Fig. 14(f)], is somewhat more difficult to visualize, since both *ortho* and *para* H_2 levels are produced by this *para* H_3 level, empirically in a ratio of approximately 2:1. The ridge so apparent in the product distributions from the $3d$ ν_0 and $3d$ ν_1 levels is less clearly formed here, but seems also to develop near $v=4$. The maximum of the population occurs around $J=7$ of $v=3$ and drops from there smoothly to all sides. An additional, weaker maximum is located at $J=7$ of $v=0$. It should be noted that the H_2 $v=14$, $J=3$ level seems to be highly populated by predissociation of the $3d$ $^2E''$ ν_2 level, and by predissociation of the $2s$ and $3s$ Rydberg levels. However, the population in this H_2 level should be viewed with caution, since its corresponding feature in the kinetic energy release spectrum could actually be produced by undiscriminated H-atom fragments produced by three-body dissociation of the H_3 levels.

Considering the very large number of H_2 rovibrational levels that are formed in the predissociation of the single H_3 Rydberg level, it is useful to characterize the entire ensemble of product energy levels by a single number. For this we define a most probable internal energy produced in the H_2 predissociation product as the average of the rovibrational level energies weighted by the squares of their observed populations. These values, expressed as a percentage of the total dissociation energy of the Rydberg level, are given in the second column of Table II. It can be seen that the values vary widely, from 8% of the available energy for the $2s$ $^2A_1'$ ν_0 level to 39% for the $3d$ $^2E''$ ν_0 level. However, a comparison of these values with the observed lifetimes of the Rydberg levels shows a clear trend: the fraction of the total available dissociation energy that appears as internal energy in the H_2 product increases as the lifetime of the predissociating H_3 level increases.

B. Comparison with theory

The most extensive *ab initio* calculations of the product distributions produced by dissociation of H_3 have been performed in two dimensions, where H_2 product rotation is neglected. In order to make a comparison between experiment and theory, product vibrational distributions were calculated from the rovibrational distributions presented in Fig. 14 by summing over the rotational populations in each vibrational level. These $H_2(v)$ product distributions are shown by the cross-hatched bars in Fig. 15. Orel and Kulander[48] performed two-dimensional wavepacket calculations and their results for the $2s$ $^2A_1'$ ν_0, and the $3d$ $^2E''$ ν_0, ν_1, and ν_2 levels are included in Fig. 14. In the theoretical treatment,[48] the shape of the Rydberg states' surfaces near their minima was assumed to be approximately the same as that of H_3^+. The adiabatic H_3 ground state surfaces of Varandas *et al.*[62] were used in the calculations, and the nonlinear coupling between the two sheets was neglected. The nonadiabatic couplings between the excited state and the ground state surfaces were assumed to be independent of the nuclear geometry. As a result of this latter assumption, any differences in the calculated product distributions of two H_3 states with the same vibrational quantum numbers can arise solely from their different total energies above the ground state surface.

Despite these limiting assumptions, the agreement between the *ab initio* product distributions and experiment is remarkably good in the cases of the $3d$ $^2E''$ ν_1 and $3d$ $^2E''$ ν_2 dissociations. In addition, the main features of the $2s$ $^2A_1'$ ν_0 distribution are also reasonably well described by theory, although theory predicts a far higher population in $H_2(v=1)$ than is actually observed, and does not reproduce the populations that are formed in very high vibrational levels of the H_2 product. In contrast, the comparison between the *ab initio* and experimental distributions for $3d$ $^2E''$ ν_0 is remarkably

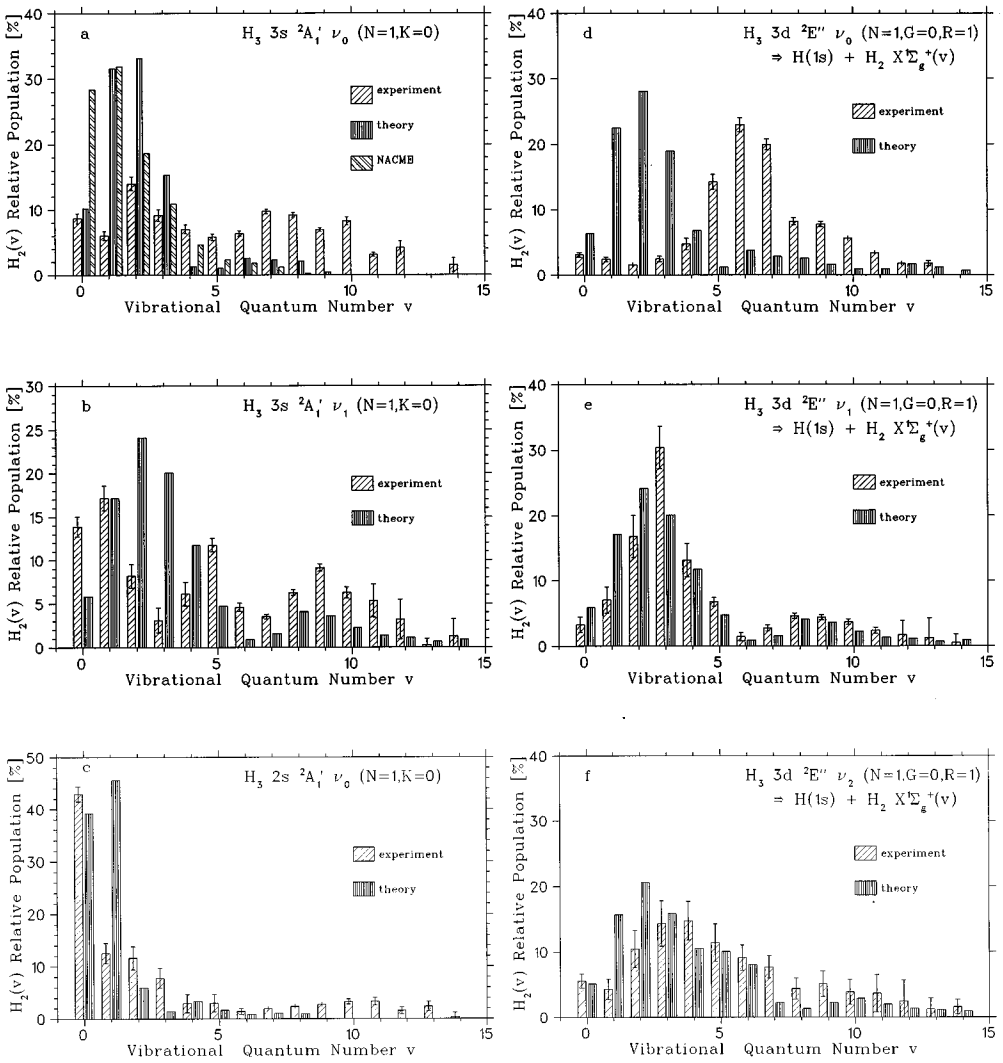

FIG. 15. Relative vibrational populations in the H_2 $^1\Sigma_g^+(v,J)$ fragments produced by predissociation of six H_3 Rydberg levels: (a) $3s\ ^2A_1'\ \nu_0$ ($N=1$, $K=0$); (b) $3s\ ^2A_1'\ \nu_1$ ($N=1$, $K=0$); (c) $2s\ ^2A_1'\ \nu_0$ ($N=1$, $K=0$); (d) $3d\ ^2E''\ \nu_0$ ($N=1$, $G=0$, $R=1$); (e) $3d\ ^2E''\ \nu_1$ ($N=1$, $G=0$, $R=1$); and (f) $3d\ ^2E''\ \nu_2$ ($N=1$, $G=0$, $R=1$). Theory denotes the results of the two-dimensional *ab initio* calculations of Krause *et al.* (Ref. 50) in (a) and of Orel and Kulander (Ref. 48) in (b)–(f) NACME indicates the *ab initio* distribution obtained when nonadiabatic coupling matrix elements describing the predissociation of the $3s\ ^2A_1'\ \nu_0$ ($N=1$, $K=0$) level were included in the calculations (Ref. 50). The theoretical distribution shown for the $3s\ ^2A_1'\ \nu_1$ level is that calculated by Orel and Kulander for the close-lying $3d\ ^2E''\ \nu_1$ level.

poor. Whereas the experimental distribution peaks near $v=6$–7, the theoretical distribution peaks at $v=2$.

Krause *et al.*[50] extended these two-dimensional calculations to the $3s\ ^2A_1'\ \nu_0$ level. Their results (Theory) together with the experimental distribution are shown in Fig. 15(a). It can be seen from this figure that the agreement between theory and experiment for this ground vibrational level is also quite poor. Whereas the experimental population is rather uniformly distributed among the H_2 vibrational levels, the *ab initio* distribution peaks strongly at $v=1$–2. It can be further noted that the *ab initio* distribution for this level is rather similar to that predicted for the $3d\ ^2E''\ \nu_0$ level. This is because these two states lie close in total energy (within 74 meV) and the theory makes no other distinction between them, since the projections of their vibrational wavefunctions onto the ground state surface are nearly identical. Yet a comparison between the experimental distributions produced by $3s\ ^2A_1'\ \nu_0$ and $3d\ ^2E''\ \nu_0$ finds that they are vastly different. This difference must arise from differences in the predissociation of these two levels, i.e., in the nonadiabatic coupling of each level to the ground state surface. Krause *et al.*[50] have made an initial investigation of this effect by calculating the nonadiabatic coupling matrix elements for the $3s\ ^2A_1'\ \nu_0$ state predissociation, in the limit of C_{2v} symmetry, and incorporating them in their two-dimensional wave packet treatment of the dynamics. Their results, labeled NACME, are shown in Fig. 15(a). It can be seen that this more realistic treatment of the predissociation did not yield a substantially better agreement between the *ab initio* product distribution and experiment, but it clearly demonstrated that the product distributions can be profoundly affected by the predissociation process. Krause *et al.*[50] have noted that substantial improvements can yet be made in the *ab initio* calculations by extending the nonadiabatic coupling calculations to a wider

TABLE II. Summary of measured and derived properties relevant to the dissociation of the H_3 Rydberg states. Column 2 lists the most probable values of H_2 product internal energy produced by two-body predissociation of the Rydberg states, expressed as a percentage of the total dissociation energy. The remaining energy appears as translation in the products. Measured ratios of rates (f_{rad}) for radiative decay into the $\tilde{X}\ 2p\ ^2E'$ ground state to total two-body predissociation are given in column 3. Also given are the rate of two-body dissociation (R_{2b}) derived from this ratio using Eq. (6) and the implied lifetime (τ_{imp}) from Eq. (7). The difference between τ_{imp} and the shorter, observed lifetime (τ_{obs}) suggests an additional decay channel which is thought to be three-body dissociation (H+H+H). The ratio of this implied three-body dissociation rate to the two-body rate is given in the last column of the table.

Rydberg Level	Product internal energy (%)	f_{rad}	R_{2b} (10^7 s^{-1})	τ_{imp} (ns)	τ_{obs} (ns)	$\frac{R_{3b}}{R_{2b}}$
$3d\ ^2E''\ \nu_0$ ($N=1$, $G=0$, $R=1$)	39	0.60	3.1	8.0	~8.0[a]	~0
$3d\ ^2E''\ \nu_1$ ($N=1$, $G=0$, $R=1$)	21	<0.37[b]	8.0	5.8	>0.4[c]	<15
$3d\ ^2E''\ \nu_2$ ($N=1$, $G=0$, $R=1$)	28	<0.31[b]	10.	5.2	⋯	⋯
$2s\ ^2A_1'\ \nu_0$ ($N=1$, $K=0$)	8	negligible	⋯	⋯	0.0002[d]	⋯
$3s\ ^2A_1'\ \nu_0$ ($N=1$, $K=0$)	32	0.09	7.1	11.9	>0.8[c],<4.0[e]	2.4–16
$3s\ ^2A_1'\ \nu_1$ ($N=1$, $K=0$)	25	(<0.15)[f]	(4.0)	(19.0)	⋯	⋯

[a]Average of lifetime measurements (Ref. 25).
[b]These values can be affected by systematic errors induced by the scaling of the laser-off spectrum.
[c]From the linewidth measurements of Ref. 47.
[d]From the linewidth measurements of Ref. 20.
[e]Reference 25.
[f]This value can be seriously affected by systematic errors induced by the scaling of the laser-off spectrum. It should be considered only with regard to its order of magnitude.

range of geometries for the H_3 and by incorporating a full three-dimensional treatment for the dissociation dynamics. The importance of a three-dimensional treatment for predicting H_3 product distributions has been demonstrated for the spontaneous radiative dissociation of the $2p\ ^2A_2''$ state.[49]

The $3s\ ^2A_1'\ \nu_1$ vibrational distribution is shown in Fig. 15(b). No explicit calculation of the *ab initio* product distribution from this state has yet been made. Therefore, for the reasons given above, we show the vibrational distribution calculated for the $3d\ \nu_1$ level[48] as theory in this figure. In contrast to the case of the ground vibrational level, the qualitative agreement between theory and experiment for the symmetric-stretch-excited level is quite reasonable.

C. Radiative decay and three-body dissociation

Besides the direct predissociation discussed above, we observe a radiative decay into the repulsive ground state surface with subsequent fragmentation into $H+H_2$ for all the $n=3$ Rydberg states investigated in this paper. Ratios between the radiative and total two-body decay, f_{rad}, as derived from the deconvolution of the kinetic energy release spectra, are given in Table II. In the case of the $3d\ ^2E''\ \nu_0$ ($N=1$, $G=0$, $R=1$) level the ratio is 60%, which is by a factor of 7 higher than the 9% observed for the $3s\ ^2A_1'$ ($N=1$, $K=0$) ν_0 level. The rates for the optically allowed transitions from the $3d\ ^2E''$ and $3s\ ^2A_1'$ states into the $\tilde{X}\ 2p\ ^2E'$ repulsive surface, calculated from the transition moments of King and Morokuma[15] (Fig. 3), are 4.7×10^7 s^{-1} and 0.7×10^7 s^{-1}, respectively, which differ by a factor of about 7 as well. This implies that the rates for the total two-particle decay of the $3s$ and $3d$ states should be about equal, in contrast to both experimental lifetime measurements[25] and the present observations of different degrees of broadening in their kinetic energy release spectra, which find the lifetime of the $3s$ state to be much shorter than that of the $3d$ state. The $3s$ level lifetime must therefore be shortened by an additional decay mechanism, which is most likely dissociation into three $H(1s)$ atoms.

Given the present radiative two-body ratio measurement, f_{rad}, the radiative decay rates from theory (Fig. 3), and an experimental lifetime for decay of the Rydberg state, τ_{obs}, we can attempt to express the importance of the three-body dissociation channel in at least qualitative terms. The rate of two-body predissociation for a given level is

$$R_{2b}=\frac{1-f_{rad}}{f_{rad}}\,R_t, \tag{6}$$

where R_t is the theoretical radiative transition rate from this level to the $\tilde{X}\ 2p\ ^2E'$ ground state. The implied lifetime of the level based on its total radiative and two-body predissociation channels is

$$\tau_{imp}=\frac{1}{R_{2b}+R_t+R_r}, \tag{7}$$

where R_r total radiative transition rate from the level into states other than the ground state. If the level has an additional decay channel of three-body dissociation with a rate R_{3b}, then its observable lifetime would be

$$\tau_{obs}=\frac{1}{R_{2b}+R_t+R_r+R_{3b}}, \tag{8}$$

and this three-body decay rate can then be estimated from

$$R_{3b}=\frac{1}{\tau_{obs}}-\frac{1}{\tau_{imp}}. \tag{9}$$

These rates, expressed as the ratio R_{3b}/R_{2b}, are given in the

last column of Table II for several of the Rydberg states for which the required lifetimes are available. It can be seen from these values that, with the exceptions of $2s\ ^2A_1'\ \nu_0$ and $3d\ ^2E''\ \nu_0$, the three-body decay rates are estimated to be comparable to, or significantly larger than, the two-body predissociation rates. Theory[50] predicts that vibrational excitation in a H_3 Rydberg level enhances its overlap with the upper sheet of the ground state surface, which adiabatically correlates to H+H+H. This seems to be supported by the estimated three-body rates for the $3d$ states given in Table II and by the dissociative charge transfer measurements of Peterson *et al.*[57] As mentioned earlier, the present photodissociation measurements also obtain direct experimental information on the three-body dissociation channel. These findings are beyond the scope of the present paper and will be presented in another publication.[53]

D. Radiative decay of the $2p\ ^2A_2''$ metastable level

As discussed in Sec. III A, several decay mechanisms are required to explain the 640 ns lifetime of the $2p\ ^2A_2''$ metastable state. A transition rate of $2\times10^4\ s^{-1}$ was estimated for the radiative transition into the $2s\ ^2A_1''$ ($N=1$, $K=0$) state from the transition frequency and the transition moments calculated by King and Morokuma.[15] This process cannot explain the observed lifetime unless the calculated transition moments are too small by two orders of magnitude. Since the rovibrational population in the $H_2(v,J)$ final state produced by predissociation of the $2s\ ^2A_1'$ state is defined by the present stimulated emission pumping experiment, we can calculate the fragment kinetic energy spectrum that should result from $2p\ ^2A_2''\leftarrow 2s\ ^2A_1''$ radiative decay.

A simulation of the fragment kinetic energy release spectrum using the experimental product populations, rather than a direct comparison to the observed stimulated emission fragment kinetic energy spectrum, is required because dissociation arising from the stimulated emission is localized to the laser interaction region, whereas that produced by spontaneous radiation can occur over the entire region between the slit and the beam flag. In calculating the apparatus function by the Monte Carlo simulation, the spatial distribution of the metastables decaying with a lifetime of 640 ns between the slit and the beam flag was explicitly taken into account. From a comparison of the simulation to the fragment kinetic energy spectrum that is produced by spontaneous dissociation of the metastable level, we estimate that radiative decay via the $2s\ ^2A_1'$ state can contribute $<4\%$ to the $2p\ ^2A_2''$ metastable decay. Direct predissociation of the metastable state by spin-orbit coupling has been estimated to account for no more than 10% of its dissociation rate.[47] It has been suggested that the primary decay channel is radiation into vibrational levels of the ground state characterized by an odd number of quanta in the degenerate (bending) mode[34] and the present findings do not alter this conclusion. The corresponding excitation process into the bending-mode-excited $3p\ ^2E'$ state has been observed following laser excitation.[36]

V. CONCLUSIONS

Photodissociation of the $2s\ ^2A_1'$ ($N=1$, $K=0$), $3s\ ^2A_1'$ ($N=1$, $K=0$) ν_0 and ν_1, and $3d\ ^2E''$ ($N=1$, $G=0$, $R=1$) ν_0, ν_1, and ν_2 states of H_3 into $H+H_2$ fragment pairs was studied using fast beam photofragment spectroscopy. Optical preparation allowed each of these Rydberg levels to be completely specified with respect to their electronic configuration and nuclear vibration, rotation, and spin. These levels are found to be predissociated, as anticipated for vibronic coupling of the H_3 excited states to the dissociative ground state. Conservation of energy in the predissociation requires that the production of a discrete rovibrational level in the H_3 dissociation product $H_2(v,J)$ also produce the discrete release of kinetic energy to the correlated pair of fragments $H+H_2(v,J)$. Explicit measurement of this kinetic energy release, by detecting both fragments produced by a single molecule with a time- and position-sensitive detector, yields a quantitative $H_2(v,J)$ product distribution for each of the referenced H_3 levels, as well as the relative probabilities for radiative decay and predissociation processes that lead to the production of $H+H_2$ fragments. The product distributions demonstrate that the production of rotational excitation and vibrational excitation in the H_2 fragment are intimately coupled by the dissociation dynamics. Qualitatively, the distributions further show that the degree of product internal excitation is inversely related to the lifetime of the predissociated H_3 state. In addition, the nuclear spin of the H_3 molecule is found not to reorient in the predissociations.

Vibrational populations in the H_2 fragment were calculated from the observed rovibrational distributions by summing over the respective rotational populations and compared with the vibrational population distributions that had been predicted from a two-dimensional *ab initio* treatment of the H_3 dissociation dynamics. While qualitative similarities are found between the experimental and *ab initio* product distributions for several of the H_3 levels, the spectacular disagreement observed for the product state distributions produced by the ground vibrational levels of the near-degenerate $3s\ ^2A_1'$ and $3d\ ^2E''$ states supports earlier suggestions[50] that explicit treatment of the nonadiabatic coupling of a H_3 Rydberg state to the ground state surface must be included for a realistic description of its dissociation dynamics.

Stimulated emission pumping of the $2p\ ^2A_2''\rightarrow 2s\ ^2A_1'$ transition allowed a detailed distribution to be determined for the predissociation products of the $2s$ state. A comparison of this distribution with that produced by the spontaneous dissociation of the $2p\ ^2A_2''$ ($N=K=0$) metastable level demonstrated unequivocally that $2p\rightarrow 2s$ spontaneous emission plays an insignificant role in the decay of the metastable level. This conclusion was anticipated by a comparison of the 640 ns measured lifetime[34] of the $2p$ level to its theoretical radiative lifetime[15,19,25] of 70 μs. The $2s\ ^2A_1'$ product state distribution also confirmed the assignment by Watson[61] of discrete energy releases observed[60] in the $H+H_2$ products of H_3^+ dissociative charge transfer in H_2 gas to the formation and predissociation of the $H_3\ 2s\ ^2A_1'$ state.

Evidence for a radiative decay into the repulsive ground

state surface with subsequent fragmentation into $H+H_2$ pairs was observed for all states investigated except for the $2s$ state, which is so rapidly predissociated that radiative decay from this state is negligible. For the referenced $n=3$ Rydberg state levels, the contribution of radiative cascade to the total production of $H+H_2$ dissociation products varied between 9% for the $3s\ ^2A_1'$ ground vibrational level to 60% for the $3d\ ^2E''$ ground vibrational level, reflecting the interplay of radiative transition rate and predissociation rate. A comparison of the fragment kinetic energy release distribution produced by radiative cascade from the $3d\ ^2E''$ level with fluorescence spectra reported[27,28] following charge transfer of an H_3^+ ion beam finds excellent agreement with the 220 nm continuum if the H_2 product is produced with little vibrational excitation, as has been predicted[49] by *ab initio* calculations. However, no evidence is found in the present work for the recently reported[28] second emission continuum centered at 320 nm, suggesting that either the H_2 product produced by dissociation on the upper sheet of the ground state surface is formed with 1 eV of internal energy or that the 320 nm continuum is produced by emission from highly excited H_3 Rydberg states.

A comparison of the presently determined ratios of radiative/predissociation decay leading to production of $H+H_2$ products with the theoretical rates for spontaneous emission and the experimental measured lifetimes suggests that dissociation into $H+H+H$ can be a very important product channel for predissociation of many of the Rydberg state levels studied here. Experimental evidence for these three-body dissociation products was obtained during the course of the present photodissociation measurements and the results will be presented in a subsequent publication.

ACKNOWLEDGMENTS

This work was partially supported by National Science Foundation Grant PHY-9111872. One of us (UM) gratefully acknowledges a fellowship from the Deutsche Forschungsgemeinshaft. We acknowledge very useful discussions with Dr. H. Helm and Dr. D. L. Huestis during the course of this work and thank Professor J. K. G. Watson for clarifying the results of his rotational linestrength calculations for us. We gratefully acknowledge the skilled assistance of Alina Dykman, who participated in this work under the Research Experience for Undergraduates program of the National Science Foundation, supported by Grant PHY-93000247.

[1] H. Eyring and M. Polanyi, Z. Physik. Chem. B **15**, 445 (1932).
[2] E. E. Marinero, C. T. Rettner, and R. N. Zare, J. Chem. Phys. **80**, 4142 (1984).
[3] D. P. Gerrity and J. J. Valentini, J. Chem. Phys. **81**, 1298 (1984).
[4] R. Goetting, H. R. Mayne, and J. P. Toennies, J. Chem. Phys. **85**, 6396 (1986).
[5] S. A. Buntin, C. F. Giese, and W. R. Gentry, Chem. Phys. Lett. **168**, 513 (1990).
[6] R. E. Continetti, B. A. Balko, and Y. T. Lee, J. Chem. Phys. **93**, 5719 (1990).
[7] L. Schnieder, K. Seekamp-Rahn, F. Liedeker, H. Steuwe, and K. H. Welge, Faraday Discuss. Chem. Soc. **91**, 259 (1991).
[8] T. N. Kitsopoulos, M. A. Buntine, D. P. Baldwin, R. N. Zare, and D. W. Chandler, Science **260**, 1605 (1993).
[9] J. C. Nieh and J. J. Valentini, J. Chem. Phys. **92**, 1083 (1990).
[10] D. E. Adelman, N. E. Shafer, D. A. V. Kliner, and R. N. Zare, J. Chem. Phys. **97**, 7323 (1992).
[11] N. C. Blais and D. G. Truhlar, J. Chem. Phys. **83**, 2201 (1985).
[12] F. Webster and J. C. Light, J. Chem. Phys. **85**, 4744 (1986).
[13] S. L. Mielke, R. S. Friedman, D. G. Truhlar, and D. W. Schwenke, Chem. Phys. Lett. **188**, 359 (1992).
[14] A. Kuppermann and Y.-S. M. Wu, Chem. Phys. Lett. **205**, 577 (1993).
[15] H. F. King and K. Morokuma, J. Chem. Phys. **71**, 3213 (1979).
[16] M. Jungen, J. Chem. Phys. **71**, 3540 (1979).
[17] R. L. Martin, J. Chem. Phys. **71**, 3541 (1979).
[18] Ch. Nager and M. Jungen, Chem. Phys. **70**, 189 (1982).
[19] I. D. Petsalakis, G. Theodorakopoulos, and J. S. Wright, J. Chem. Phys. **89**, 6850 (1988).
[20] I. Dabrowski and G. Herzberg, Can. J. Phys. **58**, 1238 (1980).
[21] G. Herzberg and J. K. G. Watson, Can. J. Phys. **58**, 1250 (1980).
[22] G. Herzberg, H. Lew, J. J. Sloan, and J. K. G. Watson, Can. J. Phys. **59**, 428 (1981).
[23] G. Herzberg, J. T. Hougen, and J. K. G. Watson, Can. J. Phys. **60**, 1261 (1982).
[24] H. Figger, Y. Fukuda, W. Ketterle, and H. Walther, Can. J. Phys. **62**, 1274 (1984).
[25] H. Figger, W. Ketterle, and H. Walther, Z. Phys. D **13**, 129 (1989).
[26] W. Ketterle, H. Figger, and H. Walther, Z. Phys. D **13**, 139 (1989).
[27] A. B. Raksit, R. F. Porter, W. P. Garver and J. J. Leventhal, Phys. Rev. Lett. **55**, 378 (1985).
[28] R. Bruckmeier, Ch. Wunderlich, and H. Figger, Phys. Rev. Lett. **72**, 2550 (1994).
[29] F.-M. Devienne, Compt. Rend. B **267**, 1279 (1968).
[30] T. Nagasaki, H. Doi, K. Wada, K. Higashi, and F. Fukuzawa, Phys. Lett. A **38**, 281 (1972).
[31] M. J. Gaillard, A. G. de Pinho, J. C. Poizat, J. Remillieux, and R. Saoudi, Phys. Rev. A **28**, 1267 (1983).
[32] G. I. Gellene and R. F. Porter, J. Chem. Phys. **79**, 5975 (1983).
[33] H. Helm, L. J. Lembo, P. C. Cosby, and D. L. Huestis, ''Photoionization and Dissociation of the Triatomic Hydrogen Molecule,'' in *Lecture Notes in Physics* (Springer, New York, 1989), Vol. 339, p. 264.
[34] C. Bordas, P. C. Cosby, and H. Helm, J. Chem. Phys. **93**, 6303 (1990).
[35] H. Helm, Phys. Rev. A **38**, 3425 (1988).
[36] L. J. Lembo, H. Helm, and D. L. Huestis, J. Chem. Phys. **90**, 5299 (1989).
[37] L. J. Lembo and H. Helm, Chem. Phys. Lett. **163**, 425 (1989).
[38] L. J. Lembo, A. Petit, and H. Helm, Phys. Rev. A **39**, 3721 (1989).
[39] C. Bordas and H. Helm, Phys. Rev. A **43**, 3645 (1991).
[40] C. Bordas, L. J. Lembo, and H. Helm, Phys. Rev. A **44**, 1817 (1991).
[41] C. Bordas and H. Helm, Phys. Rev. A **45**, 387 (1992).
[42] C. Bordas and H. Helm, Phys. Rev. A **47**, 1209 (1993).
[43] H. Helm, in *Dissociative Recombination*, edited by B. R. Crowe (Plenum, New York, 1993).
[44] A. Dodhy, W. Ketterle, H. P. Messmer, and H. Walther, Chem. Phys. Lett. **151**, 133 (1988).
[45] S. F. Selgren and G. I. Gellene, Chem. Phys. Lett. **146**, 485 (1988).
[46] P. C. Cosby and H. Helm, Phys. Rev. Lett. **61**, 298 (1988).
[47] N. Bjerre, I. Hazell, and D. C. Lorents, Chem. Phys. Lett. **181**, 301 (1991).
[48] A. E. Orel and K. C. Kulander, J. Chem. Phys. **91**, 6086 (1989).
[49] J. L. Krause, K. C. Kulander, J. C. Light, and A. E. Orel, J. Chem. Phys. **96**, 4283 (1992).
[50] J. L. Krause, A. E. Orel, B. H. Lengsfield, and K. C. Kulander, in *Time-Dependent Quantum Molecular Dynamics*, edited by J. Broeckhove and L. Lathouwers (Plenum, New York, 1992), p. 131.
[51] H. Helm and P. C. Cosby, J. Chem. Phys. **86**, 6813 (1987).
[52] D. P. de Bruijn and J. Los, Rev. Sci. Instrum. **53**, 1020 (1982).
[53] U. Müller and P. C. Cosby (unpublished).
[54] R. N. Zare, Ber. Bunsenges, Phys. Chem. **86**, 422 (1982).
[55] C. Pernot, J. Durup, J.-B. Ozenne, J. A. Beswick, P. C. Cosby, and J. T. Moseley, J. Chem. Phys. **71**, 2387 (1979).
[56] S. Datz, G. Sundström, Ch. Biedermann, L. Broström, H. Danared, S.

Mannervik, J. R. Mowat, and M. Larsson, Phys. Rev. Lett. **74**, 896 (1995).
[57] J. R. Peterson, P. Devynck, Ch. Hertzler, and W. G. Graham, J. Chem. Phys. **96**, 8128 (1992).
[58] C. Schwartz and R. J. Le Roy, J. Mol. Spectrosc. **121**, 420 (1987).
[59] W. Ketterle, H.-P. Messmer, and H. Walther, Europhys. Lett. **8**, 333 (1989).
[60] M. Vogler, Phys. Rev. A **19**, 1 (1979).
[61] J. K. G. Watson, Phys. Rev. A **22**, 2279 (1980).
[62] A. J. C. Varandas, F. B. Brown, C. A. Mead, D. G. Truhlar, and N. C. Blais, J. Chem. Phys. **86**, 6258 (1987).